

Taxanes convert regions of perturbed microtubule growth into rescue sites

Ankit Rai¹, Tianyang Liu², Simon Glauser³, Eugene A. Katrukha¹, Juan Estévez-Gallego⁴,
Ruddi Rodríguez-García¹, Wei-Shuo Fang⁵, J. Fernando Díaz⁴, Michel O. Steinmetz^{6,7},
Karl-Heinz Altmann³, Lukas C. Kapitein¹, Carolyn A. Moores² and Anna Akhmanova^{1*}

Microtubules are polymers of tubulin dimers, and conformational transitions in the microtubule lattice drive microtubule dynamic instability and affect various aspects of microtubule function. The exact nature of these transitions and their modulation by anticancer drugs such as Taxol and epothilone, which can stabilize microtubules but also perturb their growth, are poorly understood. Here, we directly visualize the action of fluorescent Taxol and epothilone derivatives and show that microtubules can transition to a state that triggers cooperative drug binding to form regions with altered lattice conformation. Such regions emerge at growing microtubule ends that are in a pre-catastrophe state, and inhibit microtubule growth and shortening. Electron microscopy and in vitro dynamics data indicate that taxane accumulation zones represent incomplete tubes that can persist, incorporate tubulin dimers and repeatedly induce microtubule rescues. Thus, taxanes modulate the material properties of microtubules by converting destabilized growing microtubule ends into regions resistant to depolymerization.

Microtubules are cytoskeletal filaments essential for numerous cellular functions. They are formed by the polymerization of tubulin dimers into a regular lattice¹. Microtubule lattices display structural plasticity, which means that they can adopt multiple conformational states with varying protofilament arrangements, curvature and extent of tube closure^{2,3}. Transitions between these states can be controlled by the nucleotide state of tubulin, by tubulin isoforms and modifications, and by local mechanical strain and binding of proteins and drugs^{2–4}.

Taxol (the brand name of the drug paclitaxel) is a microtubule-targeting agent (MTA) that is widely used for cancer therapy^{5–7}. Taxol stabilizes microtubules by binding to a luminally exposed β -tubulin site that is shared by other microtubule-stabilizing agents^{6–8}. Taxol has been shown to straighten individual microtubule protofilaments⁹, and cryo-electron microscopy (cryo-EM) analysis indicated that Taxol allosterically affects longitudinal interfaces between tubulin dimers by counteracting microtubule lattice compaction induced by guanosine triphosphate (GTP) hydrolysis^{10–12}. Furthermore, analysis of MTA interactions with unpolymerized tubulin showed that some taxane-site ligands, such as epothilone A, affect the structure of the β -tubulin M-loop, which contributes to the lateral interactions between tubulin dimers^{13–15}. The notion that taxane-site binding compounds stabilize lateral tubulin interactions is supported by a recent cryo-EM study¹⁶. While such structural insights explain how these MTAs stabilize microtubules at saturating (micromolar) concentrations, they do not account for the drug effects at lower concentrations, which potently suppress both microtubule growth and shortening⁵. Understanding such effects is of crucial importance, because they represent the clinically relevant situation as the concentration of Taxol in plasma during

chemotherapy was estimated to be in the range between tens and a few hundred nanomolar (nM)^{17–20}.

Our previous work has shown that non-saturating Taxol concentrations (50–100 nM) can promote catastrophes in vitro by the End Binding (EB) family proteins²¹. Catastrophe potentiation by low Taxol concentrations is readily observed in cells (for an example, see ref. ²²). In line with these data, low concentrations of Taxol and microtubule-destabilizing vinca alkaloids synergize rather than counteract each other in inhibiting cancer cell proliferation²³, in spite of having seemingly opposite mechanisms of action. Low Taxol concentrations thus do not increase overall microtubule stability; however, they do cause formation of discrete sites that block microtubule shrinkage and induce repeated rescues²¹. To understand how such rescue sites are formed, we visualized drug binding during microtubule growth using fluorescent taxane-site ligands. We found that these MTAs cooperatively bind to microtubule tips that are in a pre-catastrophe state and convert them into islands of stabilized microtubule lattice.

Taxane accumulations induce microtubule rescues

For direct visualization of the effects of taxanes on microtubule dynamics, we used two green fluorescent Taxol derivatives, Fchitax-3 and Flutax-2 (refs. ^{24,25}) (Supplementary Fig. 1a). We used a total internal reflection fluorescence (TIRF) microscopy-based assay, in which microtubule seeds stabilized with the slowly hydrolysable GTP analogue guanosine-5'-[(α,β)-methylene]triphosphate, sodium salt (GMPCPP) are extended in the presence of soluble tubulin with or without other proteins or drugs^{21,26} (Supplementary Fig. 1b,c). Whereas almost no rescues occurred either with tubulin alone or in the presence of mCherry-EB3, we observed frequent

¹Cell Biology, Neurobiology and Biophysics, Department of Biology, Faculty of Science, Utrecht University, Utrecht, the Netherlands. ²Institute of Structural and Molecular Biology, Birkbeck, University of London, London, UK. ³Department of Chemistry and Applied Biosciences, Institute of Pharmaceutical Sciences, ETH Zürich, Zurich, Switzerland. ⁴Chemical and Physical Biology, Centro de Investigaciones Biológicas, Consejo Superior de Investigaciones Científicas, Madrid, Spain. ⁵State Key Laboratory of Bioactive Substances and Functions of Natural Medicines, Institute of Materia Medica, Beijing, China. ⁶Laboratory of Biomolecular Research, Division of Biology and Chemistry, Paul Scherrer Institut, Villigen, Switzerland. ⁷University of Basel, Biozentrum, Basel, Switzerland. *e-mail: a.akhmanova@uu.nl

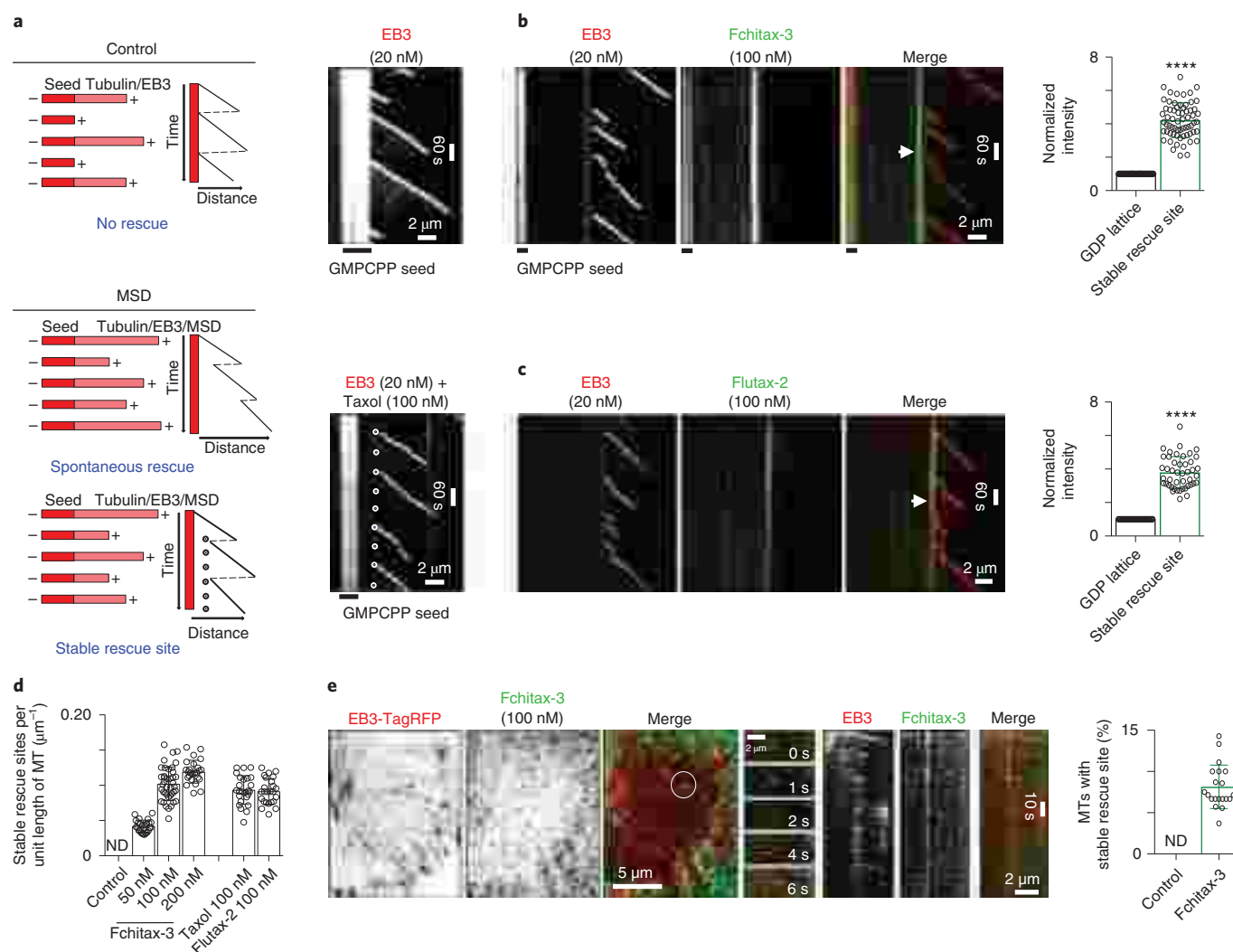


Fig. 1 | Taxol and its fluorescent derivatives induce formation of stable rescue sites in microtubules. **a–c**, Schemes illustrating in vitro microtubule growth events observed during control conditions and in the presence of microtubule-stabilizing drugs (MSD). Representative kymographs illustrate the dynamics of microtubules grown from GMPCPP seeds in the presence of 15 μM tubulin and 20 nM mCherry-EB3 without or with Taxol, Fchitax-3 or Flutax-2 (100 nM), as indicated. A stable rescue site in **a** is highlighted by a stippled white line. Note the enhanced green fluorescence of Fchitax-3 or Flutax-2 at the stable rescue site (white arrow). Bar graphs (mean \pm s.d.) show the quantification of Fchitax-3 ($n = 65$, $N = 5$ independent experiments) and Flutax-2 ($n = 45$, $N = 3$ independent experiments) intensity on both GDP lattice and stable rescue site. The values were normalized to the intensity of the GDP lattice. Error bars represent s.d. **** $P < 0.00001$, Mann-Whitney U -test. **d**, Frequency of the occurrence (mean \pm s.d.) of stable rescue sites (calculated per unit of microtubule length) at the indicated compound concentrations. ND, not detected. $n = 25$, 40 and 25 microtubules for 50, 100 and 200 nM of Fchitax-3, respectively; $n = 25$ microtubules for both Taxol and Flutax-2, three independent experiments. Error bars represent s.d. **e**, Still images, time-lapse images (corresponding to the white circle in the still image) and representative kymographs showing the formation of a dot-like Fchitax-3 accumulation corresponding to a stable rescue site in a microtubule (MT) in a HeLa cell. Bar graph (mean \pm s.d.) shows the quantification of occurrence of stable rescue sites in HeLa cells. $n = 200$ and 426 kymographs from 20 cells each for control and Fchitax-3 (100 nM)-treated sample ($N = 4$ independent experiments). Error bar represent s.d. ND, not detected.

rescues in the presence of Taxol and its fluorescent derivatives (Fig. 1a–d and Supplementary Fig. 1c–e). As described previously²¹, these rescues typically happened at defined microtubule lattice sites, which we termed ‘stable rescue sites’ (Fig. 1a–c and Supplementary Fig. 1d). Importantly, in the case of fluorescent taxanes, we observed roughly fourfold enhanced drug binding at such sites as compared to the remainder of the microtubule lattice (Fig. 1b,c). Similar sites with increased drug accumulation inducing repeated rescues could also be detected in HeLa cells that expressed EB3-TagRFP as a microtubule plus-end marker and were incubated with 100 nM Fchitax-3 for 1 h (Fig. 1e). Comparison of the intensities of single Fchitax-3 molecules and of very short Fchitax-3 accumulations at

the stable rescue sites in vitro showed that they contained ~ 15 molecules (Supplementary Fig. 1f–j). Taxane-induced formation of stable rescue sites thus occurs both in vitro and in cells, and ~ 15 drug molecules are sufficient to induce such a site.

Taxane accumulations initiate at microtubule ends

While observing microtubule growth in the presence of fluorescent taxanes, we noticed that the compounds always started to accumulate close to the growing microtubule plus- or minus-ends, directly behind the EB3-positive comet (Fig. 2a,b, Supplementary Fig. 2a and Supplementary Video 1). Taxane accumulation events appeared in a stochastic manner (Supplementary Fig. 2b) and were somewhat

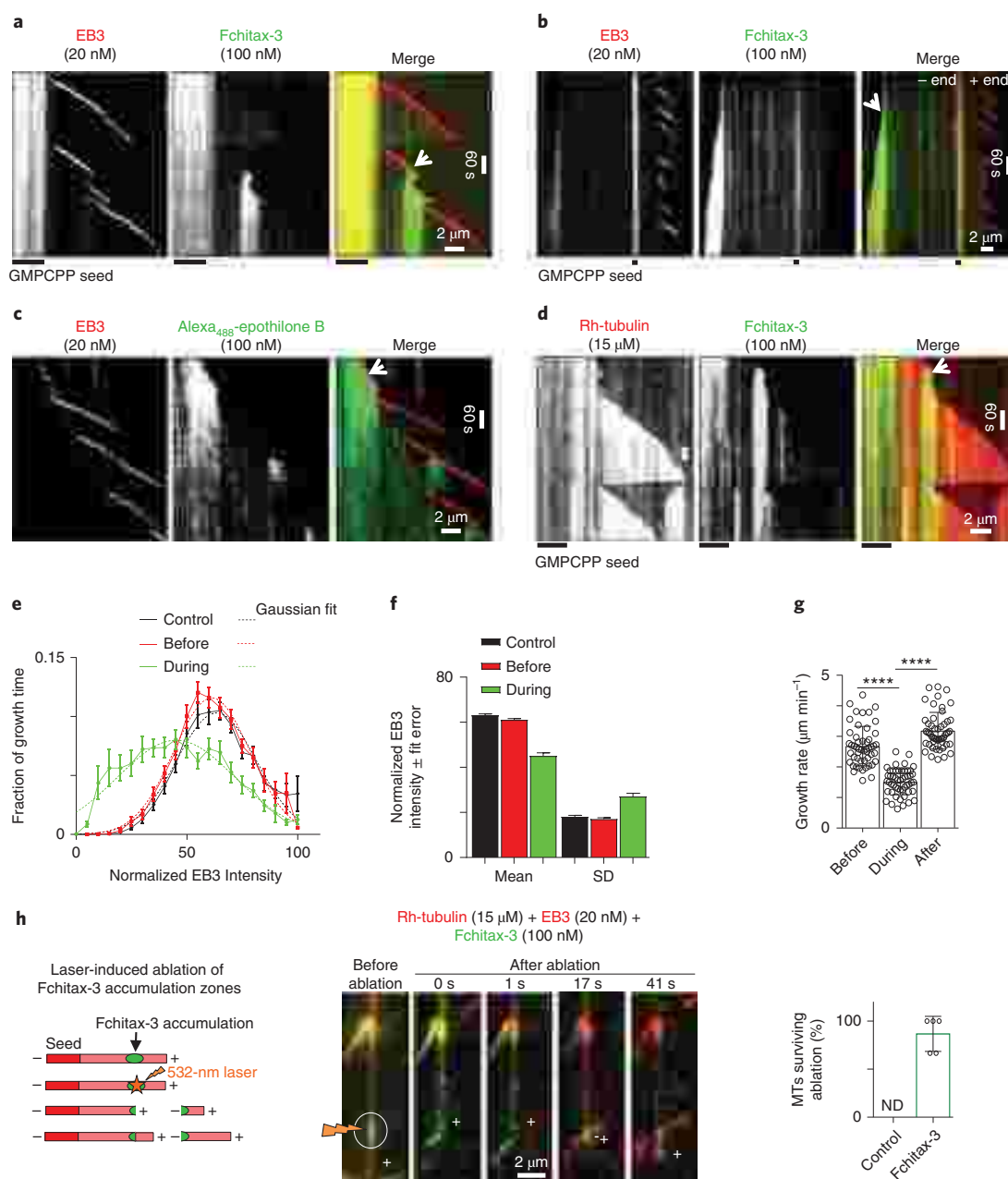


Fig. 2 | Taxane-site binding compounds accumulate at growing microtubule ends and perturb microtubule growth and depolymerization.

a–d, Kymographs, representative of three independent experiments, illustrating the accumulation of the indicated compounds at the microtubule plus- (**a,c,d**) or minus-ends (**b**) (white arrowheads in merged panels) in the presence of 15 μ M tubulin and 100 nM Fchitax-3 or Alexa₄₈₈-epothilone B, as indicated, with or without 20 nM mCherry-EB3. In **d**, 3% rhodamine-tubulin was added to the assay. **e,f**, Fluctuations in fluorescence intensity (mean \pm s.d.) of mCherry-EB3 at microtubule tips over time in control assays (15 μ M tubulin, 20 nM mCherry-EB3) or in the presence of 100 nM Fchitax-3, before or during the course of Fchitax-3 accumulation. **e**, Intensity distributions, with the experimental data denoted by solid lines and Gaussian fits by dotted lines, $n=30$ for control and $n=25$ for Fchitax-3-treated sample, $N=3$ independent experiments. **f**, Plots of mean and s.d. values of the Gaussian fits. **g**, Microtubule growth rate (mean \pm s.d.) in the presence of 15 μ M tubulin, 20 nM mCherry-EB3 and 100 nM Fchitax-3 before, during and after Fchitax-3 accumulation. $n=51$ in each case, $N=3$ independent experiments, error bars represent s.d.; **** $P < 0.0001$ (growth rate during accumulation was compared to those before and after Fchitax-3 accumulation), Mann-Whitney U -test. **h**, Schematic representation and still images of laser ablation of a microtubule (MT) with a Fchitax-3 accumulation zone, observed in the presence of 15 μ M tubulin (supplemented with 3% rhodamine-tubulin), 20 nM mCherry-EB3 and 100 nM Fchitax-3. The ablated microtubule region is highlighted by a lightning bolt and white circle. The positions of the plus- and minus-ends of the microtubule are indicated. Quantification (mean \pm s.d.) of microtubule survival after ablation in control conditions (no drug) or within a Fchitax-3 accumulation zone ($n=15$ microtubules from five independent experiments) is shown on the right. ND, not detected.

more prolonged and more frequent at the minus-ends (Fig. 2a,b and Supplementary Fig. 2a,c). For subsequent work, we focused on drug accumulations at the plus-ends, as minus-ends typically do

not significantly elongate in vivo²⁷. Consistent with the in vitro data, transient accumulations of Fchitax-3 were also observed at growing microtubule plus-ends in cells (Supplementary Fig. 2d,e).

To test whether end-dependent binding is specific for Taxol analogues, we generated an Alexa-488-labelled derivative of epothilone B (Supplementary Fig. 1a and Supplementary Fig. 3a,b), a different taxane-site binder, and found that it exhibited similar accumulations at growing microtubule ends (Fig. 2c). Drug accumulations also occurred in the absence of EB3 (Fig. 2d and Supplementary Fig. 2f); however, since EBs facilitate the detection of growing microtubule tips, subsequent experiments were carried out in the presence of EB3. During periods of strong drug accumulation, microtubule growth was perturbed, as could be seen by the reduction of EB3 signal and the microtubule growth rate (Fig. 2a,c–g). After a brief interval, an accumulation could abruptly stop and normal microtubule growth was resumed (Fig. 2a,c–g). Concomitantly, the region of enhanced drug binding persisted in the microtubule lattice (Fig. 2a,c,d). If such a growing microtubule started shrinking, microtubule depolymerization was arrested within the region with a high drug concentration, leading to rescue, which was often observed repeatedly at the same site (Fig. 2a,c and Supplementary Fig. 2a). Microtubule polymerization, with periods of perturbed growth and subsequent frequent rescues initiating within the same microtubule region, was also observed with Taxol with and without EB3 (Supplementary Fig. 2g,h). Such a behaviour is thus representative for taxane-site MTAs and is not an artefact of fluorescently labelled drugs.

To confirm that regions with high taxane accumulation have increased stability, we performed laser-severing experiments. Whereas control microtubules always depolymerized at the newly generated plus- and minus-ends (Supplementary Fig. 2i), the presence of a Fchitax-3 accumulation prevented shrinkage of freshly severed ends (Fig. 2h and Supplementary Video 2). These data demonstrate that increased taxane incorporation initiated close to a growing microtubule end leads to stabilization of a stretch of microtubule lattice.

Growth perturbations trigger taxane accumulations

Since microtubule minus-ends grow more slowly than plus-ends and show longer and more frequent Fchitax-3 accumulations (Supplementary Figs. 1c and 2c), we initially hypothesized that drugs can accumulate more easily at their luminal binding sites if microtubule polymerization is slow. However, when we varied tubulin concentration to alter the growth rate (Supplementary Fig. 4a,b), we found that Fchitax-3 accumulations became more frequent when microtubules grew more rapidly (Fig. 3a,b and Supplementary Fig. 4c). At higher growth rates, the length of Fchitax-3 accumulations increased (Fig. 3a,b and Supplementary Fig. 4c). In our assays, in the presence of EB3 without MTAs, increased tubulin concentrations led to a higher catastrophe frequency although at 25- μ M tubulin we did observe some microtubules that were persistently elongating (Supplementary Fig. 4a); importantly, such microtubules still displayed frequent growth perturbations that appeared as a catastrophe followed by a rapid rescue (Supplementary Fig. 4a,b).

Interestingly, we noticed that Fchitax-3 accumulations were often initiated when microtubule polymerization appeared sub-optimal or perturbed, which was often observed at microtubule minus-ends (Supplementary Figs. 1c and 2b), or when the plus-end of a GMPCPP seed had just started to elongate (Supplementary Fig. 4d). Fchitax-3 accumulation events were always accompanied by a decrease in microtubule growth rate and concomitant loss in EB3 signal (Fig. 2e–g). Analysis of the onset of such events with a higher temporal resolution, and careful alignment of the Fchitax-3 and EB3 channels, showed that on processively growing microtubules the appearance of a new Fchitax-3 accumulation occurred ~5 s after a clear reduction in EB3 signal (Fig. 3c–e). Reduction in the number of EB3-binding sites at the growing microtubule end is a hallmark of the pre-catastrophe state²⁸ (Supplementary Fig. 4e). Furthermore, the frequencies of catastrophes and of the appearance

of Fchitax-3 accumulations at the growing microtubule ends are similar (Supplementary Fig. 4f).

We therefore wondered whether Fchitax-3 accumulations could be triggered by changes in the microtubule end conformation that lead to catastrophe. Catastrophes can potentially be stimulated in our *in vitro* assays by different microtubule-depolymerizing agents, such as vinblastine²¹, or by kinesin-13 family protein mitotic centromere-associated kinesin (MCAK)²⁹. The addition of either vinblastine or GFP-MCAK, which specifically tracked growing EB3-positive microtubule ends, reduced microtubule growth rate and indeed promoted catastrophes (Supplementary Fig. 4g). These conditions are somewhat similar to the dynamics of microtubule minus-ends, which exhibit frequent growth perturbations (Supplementary Figs. 1c and 4g). Interestingly, the addition of vinblastine or GFP-MCAK increased the frequency of Fchitax-3 or Alexa₄₈₈-epothilone B accumulations, as well as the occurrence of stable rescue sites with or without EB3 (Fig. 3f–i and Supplementary Fig. 4h,i). A similar pattern of microtubule plus-end growth with frequent perturbations and repeated rescues was also observed with the combination of vinblastine and Taxol (Fig. 3j), indicating that the behaviour of fluorescent compounds is representative for taxane-site binders. It should be emphasized that vinblastine can bind to both free tubulin and the outermost microtubule tips³⁰, but cannot be incorporated into microtubule lattices or directly influence the conformation of the taxane-binding site within microtubule shafts. MCAK also acts at the outermost microtubule tips and is not expected to influence microtubule lattice structure³¹. Together, these data show that the perturbed structure of a microtubule end associated with the pre-catastrophe state induces the formation of lattice regions with enhanced taxane accumulation.

Analysis of Fchitax-3-binding kinetics

To understand better how Fchitax-3 accumulations are formed, we analysed their dynamics in more detail. After initiation of binding, Fchitax-3 intensity on the microtubule first rapidly increased over the course of ~50 s and then, after a period of ~100 s, it abruptly started to diminish (Fig. 4a). The rapid decline in Fchitax-3 intensity within the accumulation zone was not caused by photobleaching (Supplementary Fig. 5a, see figure legend for details), and thus was due to drug dissociation from the microtubule.

The shape of the kinetic curve, with a rapid rise and subsequent decline, suggests that some tubulin dimers first acquire an ability to bind Fchitax-3 (the initial drug accumulation phase) but later are converted to a state lacking this ability (the drug desorption phase). Because Fchitax-3 binding does not happen throughout the entire period of microtubule growth but emerges at the ends that are in a pre-catastrophe state, we defined two subsets of tubulins present at microtubule ends, which have varying ability to interact with Fchitax-3: $Tu^{\text{receptive}}$ and $Tu^{\text{unreceptive}}$. To account for desorption, we assumed that these states can be turned into the microtubule lattice-specific conformational state that does not bind to Taxol under these conditions (Tu^{lattice}).

To model the kinetics of Fchitax-3 accumulation and unbinding, we first used a Michaelis–Menten type of model in which Taxol was taken as a catalyst that binds $Tu^{\text{receptive}}$ (the substrate) that subsequently converts irreversibly to a non-Taxol-binding state within the microtubule lattice (Tu^{lattice} , the product). However, this model provided a poor fit to the experimentally obtained binding curve (Fig. 4b,c and Supplementary Fig. 5b,c). To account for the rapid and sustained increase in drug accumulation, we introduced an autocatalytic step (Fig. 4b) in which binding of Taxol to $Tu^{\text{receptive}}$ can trigger the conversion of unreceptive tubulin at microtubule ends to receptive tubulin (Fig. 4a–c and Supplementary Fig. 5d–g; see Methods for details). The obtained rate constant of Fchitax-3 binding (k_1 , $5.6 \pm 0.5 \times 10^5 \text{ M}^{-1} \text{ s}^{-1}$) was in good agreement with previously reported measurements for Flutax-1 and Flutax-2 (refs. ^{24,32}),

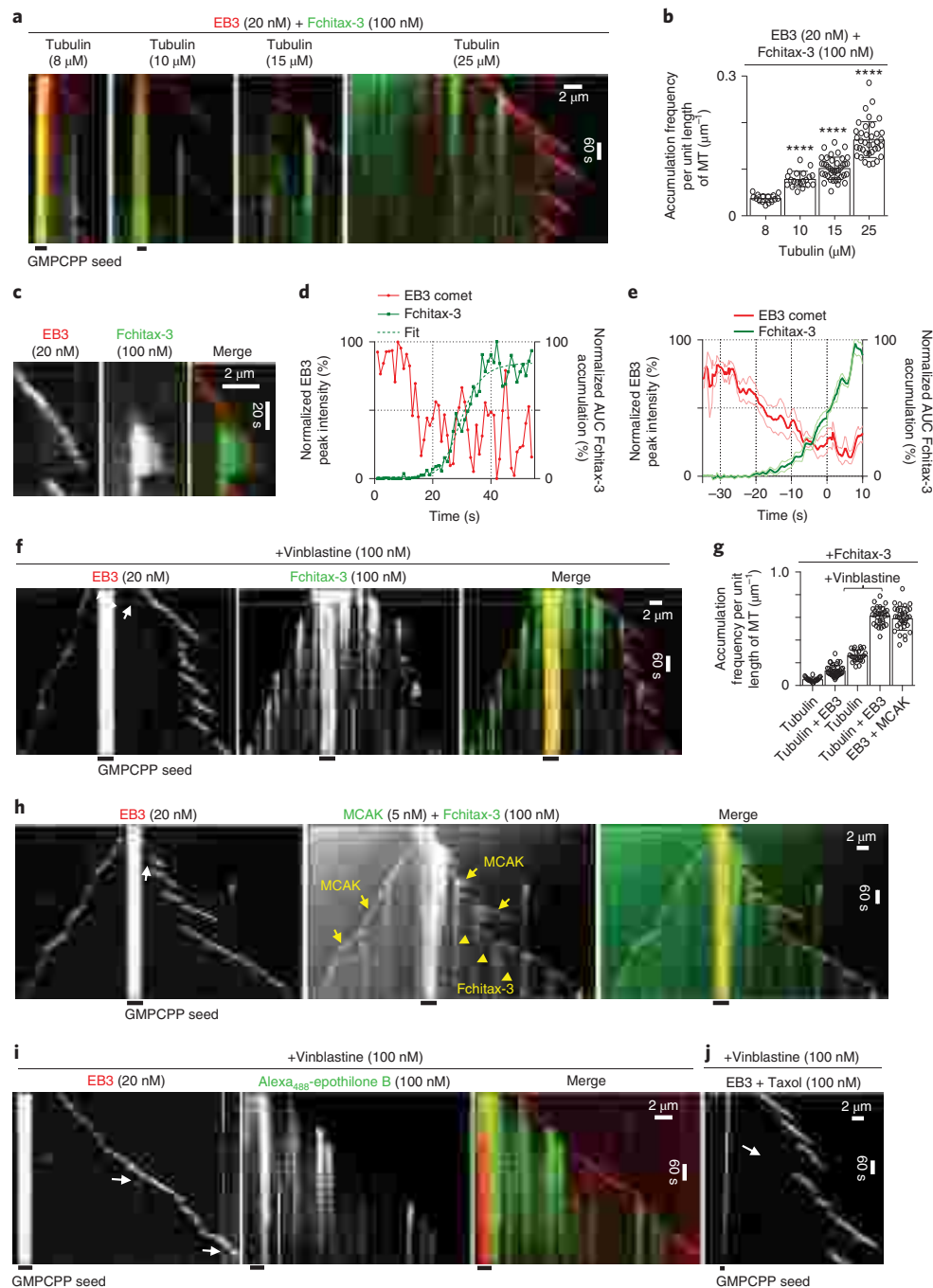


Fig. 3 | Formation of accumulations of taxane-site ligands is controlled by microtubule dynamics. **a**, Kymographs, representative of three independent experiments, showing Fchitax-3 accumulations in microtubules grown in the presence of the indicated tubulin concentrations, 20 nM mCherry-EB3 and 100 nM Fchitax-3. **b**, Quantification of Fchitax-3 accumulation frequency (mean \pm s.d.) for the experiments shown in **a**. $n = 15, 20, 40$ and 37 accumulations in $250, 185, 135$ and 94 growth events for $8, 10, 15$ and 25μ M of tubulin, respectively. $N = 3$ independent experiments, error bars represent s.d., **** $P < 0.0001$, Mann-Whitney U -test. **c**, Kymograph showing the initiation of a Fchitax-3 accumulation associated with the reduction in mCherry-EB3 signal. $n = 5$, experimental conditions as in **a**. **d**, Time plot of the normalized maximum intensity of a fitted EB3 comet (red) and the normalized area under the curve (AUC) of a fitted Fchitax-3 (green) intensity profile. The dashed green line shows the fit of Fchitax-3 kinetics to a Hill equation (on x axis, time was used rather than concentration), representative of five experiments. **e**, Averaged EB3 and Fchitax-3 profiles (as in **d**), normalized and aligned using half-maximum effective concentration (EC_{50}) values from Hill equation fits as reference points (nine kymographs from five experiments). **f, h–j**, Kymographs (representative of three experiments) illustrating microtubule dynamics in the presence of 15μ M tubulin, 20 nM mCherry-EB3 and 100 nM vinblastine with 100 nM Fchitax-3 (**f**), or 100 nM Alexa₄₈₈-epothilone B (**i**), or 100 nM Taxol (**j**). Panel **h** shows microtubule dynamics in the presence of 15μ M tubulin, 20 nM mCherry-EB3 with 100 nM Fchitax-3 and 5 nM MCAK. Note that GFP-MCAK at growing microtubule ends and Fchitax-3 accumulations are detected in the same channel. White arrows highlight EB3 comets emerging from the accumulation zones and moving in the reverse direction. **g**, Quantification of Fchitax-3 accumulation frequencies (mean \pm s.d.) per microtubule unit length in the presence of 15μ M tubulin ($n = 22$), 20 nM mCherry-EB3 ($n = 40$), 15μ M tubulin with 100 nM vinblastine ($n = 25$), 20 nM mCherry-EB3 with 100 nM vinblastine ($n = 30$) and 20 nM mCherry-EB3 with 5 nM MCAK ($n = 34$). n , number of microtubules, $N = 3$ independent experiments, error bars represent s.d.

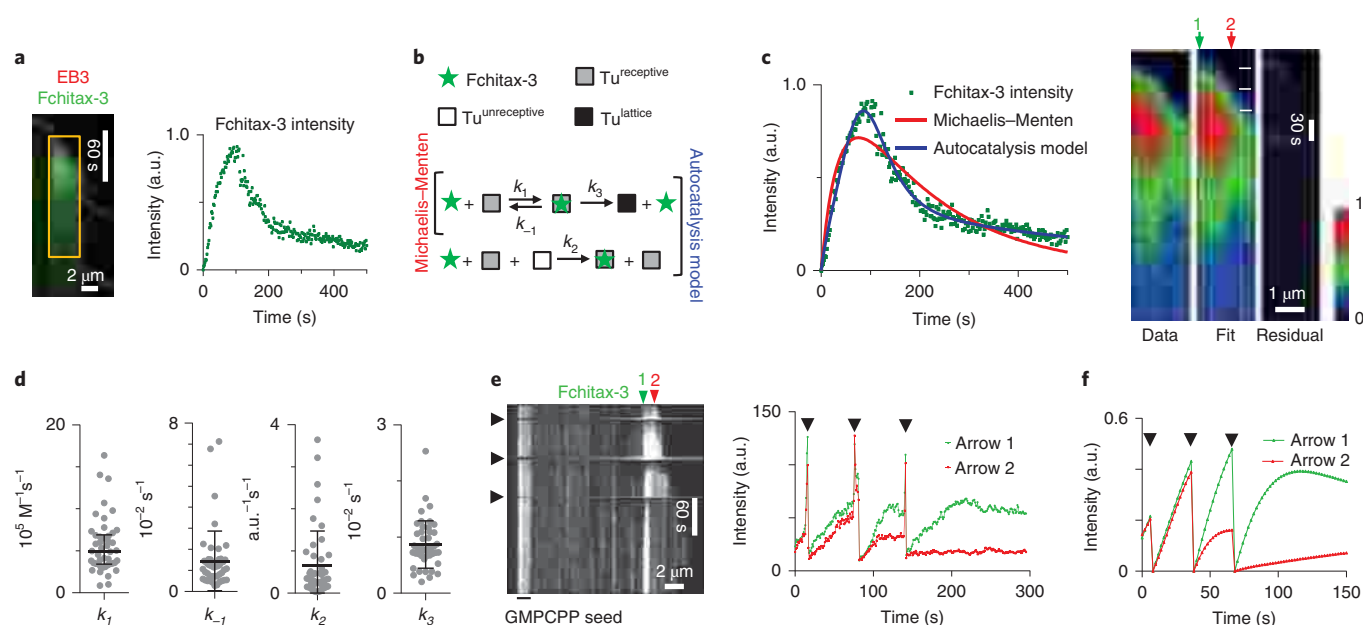


Fig. 4 | Analysis of the kinetics of Fchitax-3 accumulations. **a**, Kymograph, representative of five independent experiments, with a long Fchitax-3 accumulation (left) and a line intensity time trace of Fchitax-3 at the beginning of the accumulation (right). a.u., arbitrary units. **b**, Schematic kinetic diagram of the Michaelis-Menten (top reaction) and autocatalysis (top and bottom reactions) models for Fchitax-3 binding. Three tubulin states are considered: initial state unable to bind Fchitax-3 ($Tu_{unreceptive}$), Fchitax-3-binding state ($Tu_{receptive}$) and final converted state ($Tu_{lattice}$) (again, unable to bind Fchitax-3). For more details see Methods. **c**, Left: best fits to a single profile shown in **a** using either Michaelis-Menten (red line) or the autocatalysis model (blue line). Right: raw data, best fits and residuals of the autocatalysis model to the area of the kymograph bounded by a yellow rectangle in **a**. Arrows 1 and 2 indicate the positions along the microtubule for which FRAP was modelled in **f**, with white dashes indicating the moments of photobleaching used for calculation of the modelled curves. **d**, Rate constants (mean \pm s.d.) of kinetic autocatalysis model (**b**) derived from intensity time trace fits (nine kymographs, 46 time traces). Error bars represent s.d. **e**, Left: kymograph of three sequential photobleaching events (highlighted by black arrowheads) of a Fchitax-3 accumulation. Right: intensity time traces along the lines marked by arrows 1 and 2 in the kymograph. Kymograph and intensity time traces are representative of three independent experiments. **f**, Modelling of FRAP curves: solutions of the model for fluorescence recovery with parameter values from fits shown in **c** (right), where the moments of photobleaching are indicated by white dashes. The same photobleaching moments are indicated by black arrowheads in **f**.

whereas the rate constant of dissociation was an order of magnitude lower (k_{-1} , $1.4 \pm 0.2 \times 10^{-2} \text{ s}^{-1}$; Fig. 4d). This is consistent with the fact that the affinity of Fchitax-3 for its binding site is an order of magnitude higher than that of Flutax-2 (refs. 24,25).

Next, we explored how the kinetic parameters changed along the length of the microtubule zone where an accumulation happened. In our dynamics assays, maximum Fchitax-3 intensity observed over time was typically higher at the initial point of accumulation compared to its distal end, which was formed later (Fig. 4a). In the model, this was reflected by the diminishing number of tubulin dimers per unit of microtubule length that could interact with the drug (Supplementary Fig. 5d). Furthermore, fluorescence recovery after photobleaching (FRAP) data showed that the recovery of Fchitax-3 at the starting point of an accumulation was higher compared to that at the distal end of an accumulation (Fig. 4e), and this fitted well with the modelling results (Fig. 4c,f). The higher number of drug-binding sites at the starting point of Fchitax-3 accumulation was in agreement with the observation that this region was often most resistant to depolymerization (see Fig. 3c for an example). Thus, the conformation of the microtubule zone with high taxane affinity was changing along the growing microtubule. This could have been due to certain global alterations in microtubule geometry, such as gradual closure of an open tubulin sheet. In the model, this was reflected by the variability of the autocatalysis rate constant k_2 (Fig. 4d), which can be expected to be affected by tubulin conformation in the microtubule lattice.

Quantification of the density of Fchitax-3 molecules during maximal accumulation along microtubule stretches of $\sim 900 \text{ nm}$ in

length showed that only one or two drug molecules were bound per 8 nm, the length of one tubulin dimer (Supplementary Fig. 5h). Since GMPCPP-nucleated microtubules in our assays are expected to have ~ 14 protofilaments, this means that even at the highest binding density the microtubule is still far from being saturated with the drug. It should be noted that, since this quantification is based on the average fluorescence intensity, it is possible that Fchitax-3 molecules are distributed in an irregular fashion—for example, with neighbouring tubulin subunits being preferentially in either bound or unbound state. Combined with the modelling, our data suggest that taxanes display cooperative binding to microtubules even at low saturation, implying that changes in drug-binding affinity can propagate in microtubule lattices.

Nucleotide state of tubulin affects Fchitax-3 binding

Since growing microtubule ends maintain a GTP cap that is gradually hydrolysed, and because tubulin undergoes nucleotide-dependent conformational changes^{10,16,33}, enhanced Fchitax-3 binding at growing microtubule tips could be due to a particular nucleotide state. Fchitax-3 and other tested taxanes indeed showed preference for GMPCPP seeds and GMPCPP-containing microtubule extensions as compared to guanosine-5'-diphosphate (GDP)-bound lattices (Fig. 5a,b). FRAP analysis of Fchitax-3 signal on GMPCPP seeds provided an estimate for the dissociation constant (k_{-1} FRAP, $2.2 \pm 0.3 \times 10^{-2} \text{ s}^{-1}$), which was similar to the values derived from our autocatalysis kinetic model (Fig. 5c,d). In contrast, Fchitax-3 had no preference for guanosine 5'-O-[gamma-thio]triphosphate (GTP γ S)-bound microtubules, which are thought to mimic the

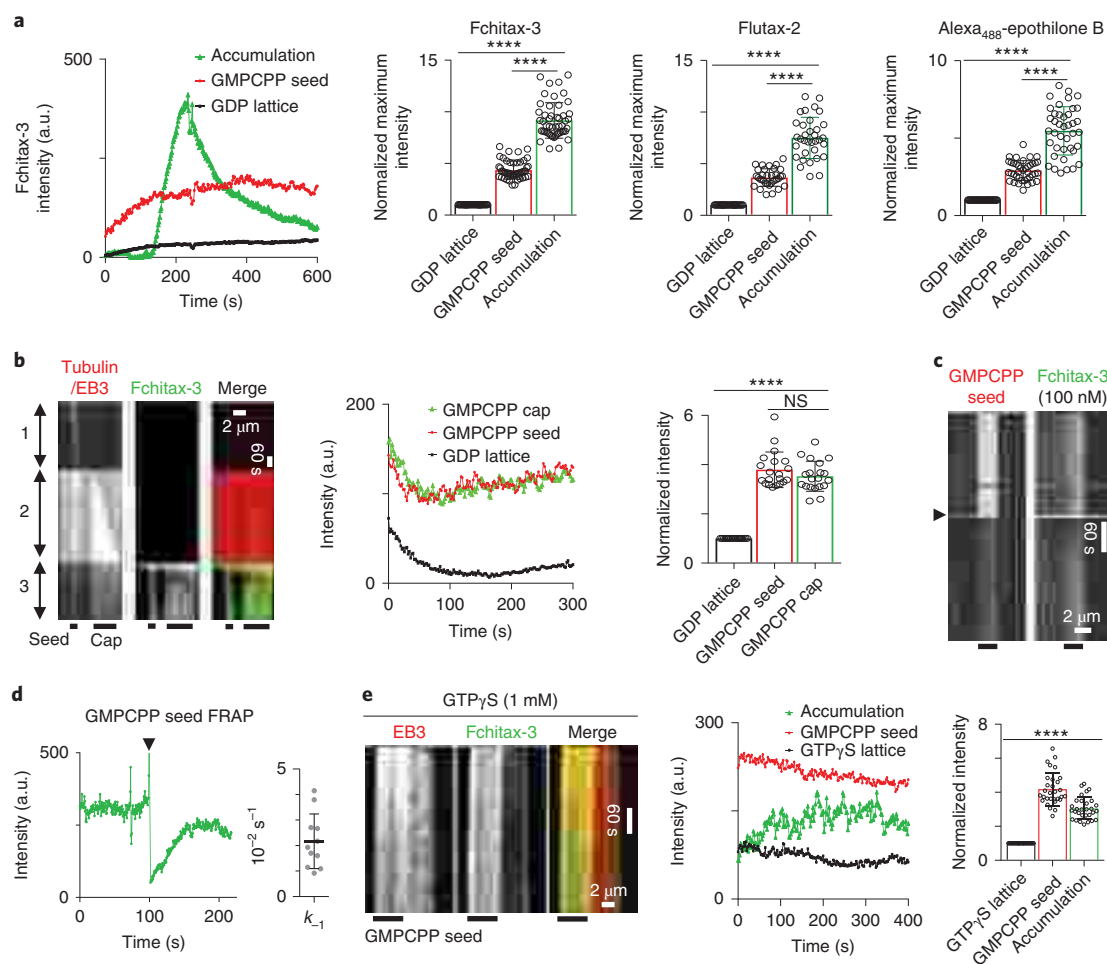


Fig. 5 | Analysis of the nucleotide dependence of Fchitax-3 accumulations. **a**, Fchitax-3 (100 nM) fluorescence intensity profile on GMPCPP-stabilized microtubule seed, dynamic microtubule lattice (GDP lattice) and within a Fchitax-3 accumulation. Bar graphs (mean values) show quantification of the normalized maximum value of fluorescence intensity on GMPCPP-stabilized microtubule seed, GDP lattice and within a Fchitax-3 ($n=50$, $N=5$), Flutax-2 ($n=34$, $N=3$) or Alexa₄₈₈-epothilone B ($n=40$, $N=3$) accumulation zone. The values were normalized to the intensity of the GDP lattice. Error bars represent s.d. **** $P < 0.0001$, Mann-Whitney U -test. **b**, Kymographs illustrating in vitro dynamics of a microtubule that was first grown from a GMPCPP seed in the presence of 15 μ M tubulin and 20 nM mCherry-EB3 (1), in the presence of 5 μ M tubulin supplemented with 3% rhodamine-tubulin and 250 μ M GMPCPP (GMPCPP cap) (2) and then incubated with 100 nM Fchitax-3 (3). Fluorescence intensity profiles and Fchitax-3 intensities (mean) normalized to the intensity of the GDP lattice are shown on the right. $n=20$, $N=3$ independent experiments. Error bars represent s.d., **** $P < 0.0001$; NS, not significant, $P=0.25$, Mann-Whitney U -test. **c,d**, Representative kymographs, single-line intensity time traces and plot (mean value) showing the rate constant of photobleaching of Fchitax-3 within GMPCPP seeds. $n=11$, $N=5$ independent experiments. Error bar represents s.d. Black arrowhead indicates the time point when photobleaching was performed. **e**, Representative kymographs, intensity profiles and a plot (mean) showing quantification of the intensity of Fchitax-3 fluorescence for GMPCPP-stabilized seed, microtubule lattice grown in the presence of 15 μ M tubulin, 20 nM mCherry-EB3, 1 mM GTP γ S and 100 nM Fchitax-3 (GTP γ S lattice) and the Fchitax-3 accumulation zone within the same microtubule. Intensity values were normalized to the intensity of the GTP γ S lattice. $n=30$ from $N=3$ independent experiments, error bars represent s.d., **** $P < 0.0001$, Mann-Whitney U -test.

GTP hydrolysis intermediate GDP-inorganic phosphate (GDP-Pi) state of tubulin^{11,33} (Fig. 5e).

Preferential binding to GMPCPP microtubules might be due to their longitudinally extended lattice conformation, because Taxol was reported to induce similar microtubule lattice extension when added during, though not after, microtubule assembly^{11,16,33,34}. To gain support for the idea that Taxol affects tubulin dimer length within microtubules, we performed X-ray fibre diffraction experiments with microtubules that were assembled from GTP-tubulin and were either untreated or treated with Taxol during or after polymerization (Supplementary Fig. 6a–e). Both Taxol-treated samples exhibited increased dimer length compared to drug-free microtubules, though this length was slightly shorter in samples treated with Taxol after assembly (Supplementary Fig. 6f,g). Similarly, microtubules

assembled from GDP-tubulin incubated with Taxol during polymerization also displayed extended lattice (Supplementary Fig. 6d–g) (note that GDP-tubulin does not polymerize without Taxol and, therefore, the effect of Taxol could not be tested under post-assembly conditions). Taxol can thus induce changes in microtubule lattice compaction that could contribute to the observed binding preferences and cooperativity. However, the maximum intensity of Fchitax-3 accumulations at microtubule ends greatly exceeded the intensity of the drug binding to GMPCPP-stabilized seeds present in the same microtubules (Fig. 5a). Furthermore, Fchitax-3 accumulations could also form at microtubule tips in the presence of GTP γ S, although in this case their intensity was typically lower than that at GMPCPP-containing microtubule seeds in the same assay (Fig. 5e). We therefore conclude that the nucleotide state of tubulin

and the associated changes in the longitudinal lattice compaction can affect taxane binding, but that they are not sufficient to explain the strong drug accumulations at microtubule ends. In particular, rapid release of Fchitax-3 from the accumulation zones and the abrupt transitions between regions of high and low drug binding can best be explained by additional global conformational transitions, such as the closure of a microtubule sheet into a tube.

Taxanes induce tube closure defects

To investigate whether the presence of taxane accumulations is indeed associated with deviations in microtubule structure, we performed cryo-EM analysis of GMPCPP-stabilized microtubule seeds, control microtubules, microtubules grown in the presence of either Fchitax-3 or vinblastine, or both agents together (Fig. 6a–d and Supplementary Fig. 7a–c). GMPCPP-stabilized microtubule seeds showed a regular geometry with very few, small defects (≤ 40 nm) (Supplementary Fig. 7a). Whereas Fchitax-3 had no effect on the abundance of small microtubule defects (≤ 40 nm), we observed in its presence a significant increase in the frequency of incomplete microtubule shaft regions >40 nm (Fig. 6a–d). Very long regions of incomplete microtubule lattices were seen when Fchitax-3 and vinblastine were combined (Supplementary Fig. 7b,c). These data strongly suggest that the regions of enhanced Fchitax-3 binding represent microtubule regions that failed to close into a complete microtubule tube.

Incomplete microtubule lattice structures are expected to show increased flexibility, and we indeed observed a strong increase in transverse microtubule tip fluctuations during the formation of Fchitax-3 accumulations (Fig. 6e). It should be noted that Taxol binding can, per se, reduce microtubule rigidity^{34–36} and it is possible that this effect contributes to the flexible character of the Fchitax-3 accumulation zones.

To confirm that Fchitax-3-grown microtubules contain interrupted protofilaments, we used as a tool the microtubule minus-end-binding protein CAMSAP3. CAMSAPs recognize free microtubule minus-ends because their signature domain, CKK, binds in a minus-end-specific manner to interprotofilament sites at uncapped microtubule extremities³⁷. Interestingly, distinct CAMSAP3 binding was observed at $\sim 30\%$ of Fchitax-3 accumulations (Fig. 6f and Supplementary Fig. 7d). Over time, the CAMSAP3 signal extended in the minus-end direction (Fig. 6f). Since CAMSAPs decorate growing microtubule minus-ends³⁸, these data indicate that

Fchitax-3 accumulations can create regions of incomplete microtubule lattice that can be extended by tubulin addition. These data also explain why Fchitax-3 accumulation zones can serve as the origin of EB3-positive comets (Fig. 3f,h, white arrows in EB3 panels), which highlight growing protofilament plus- and minus-ends. Similar events were also observed in the presence of Taxol (Fig. 3i, white arrows).

Next, we used FRAP assays in the tubulin channel to test for tubulin incorporation at the Fchitax-3 accumulation zones. Whereas control microtubule lattices showed no fluorescence recovery (Supplementary Fig. 7e), Fchitax-3 accumulation zones displayed clear recovery of the tubulin signal (Fig. 6g). In some cases, the length of tubulin incorporation detected after photobleaching was up to $\sim 1 \mu\text{m}$ (Supplementary Fig. 7f). We also frequently observed transient binding of EB3, a marker of growing microtubule ends, within the drug accumulation areas (Fig. 6h and Supplementary Fig. 7g). These data indicate that tubulin indeed incorporates into microtubule lattice within Fchitax-3 accumulation zones. Such microtubule repair explains why the length of microtubule lattice defects observed by electron microscopy (~ 100 nm) was much shorter than that of Fchitax-3 accumulation zones, which could extend to several micrometres (compare Fig. 6d and Supplementary Fig. 7h). These results indicate that the formation of Fchitax-3 accumulations is associated with major microtubule lattice defects, such as missing parts of protofilaments that are partly restored by tubulin incorporation.

Discussion

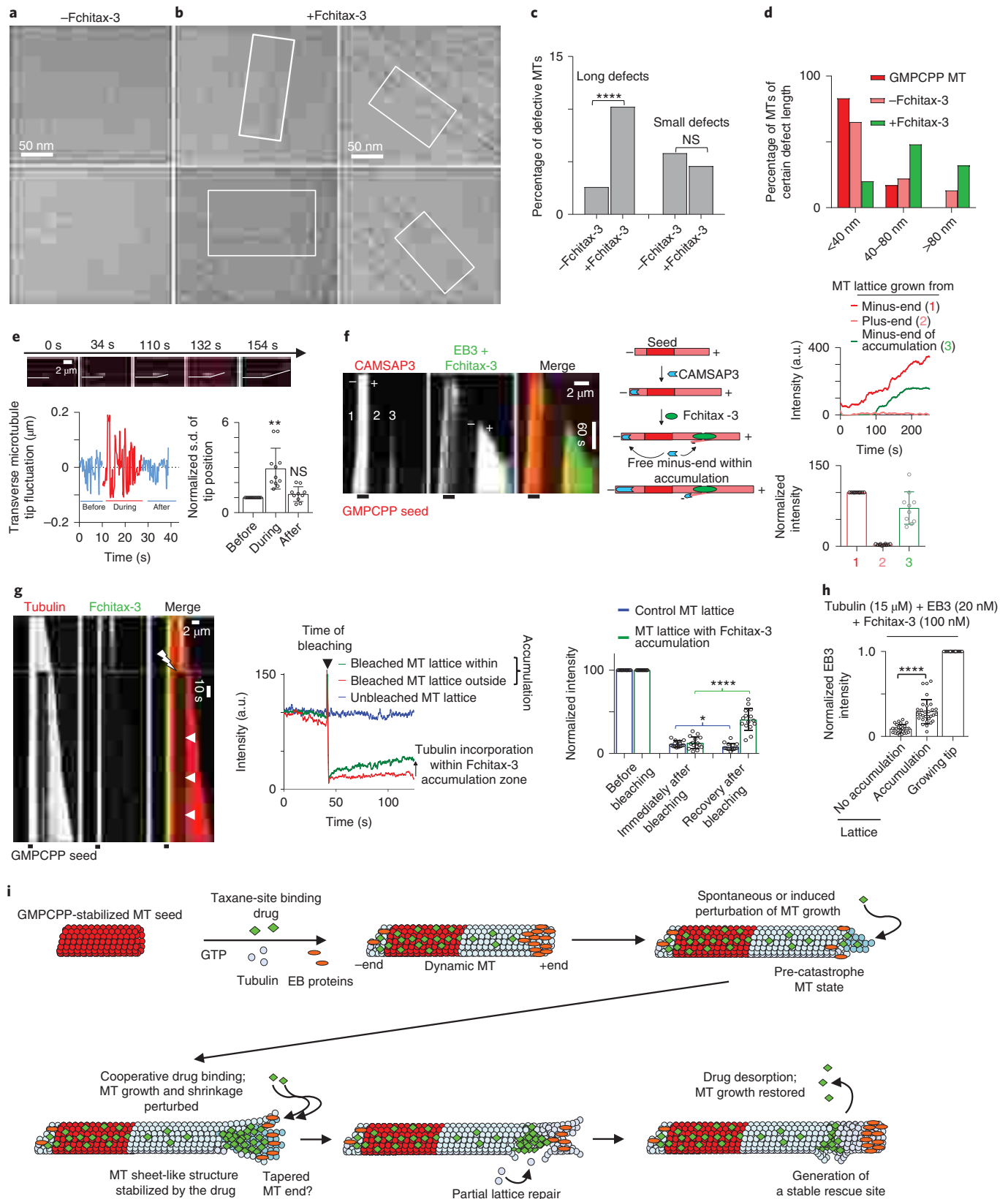
In this study, we found that the association of taxane-site ligands with microtubules preferentially occurs at growing microtubule ends and is strongly dependent on the conformational state of these ends, leading to a highly uneven binding pattern along the microtubule shaft. This observation helps to explain why taxane-site ligands have a stronger effect on microtubule lattice structure when added during, and not after, microtubule polymerization^{34,39}. Previous models of Taxol stabilization mechanisms assumed a stochastic but homogeneous change in the rate constants and thermodynamic states of tubulin dimers within a microtubule⁴⁰. In contrast our data show that, at non-saturating concentrations of the compound, microtubule stabilization is achieved by the formation of specific zones (local ‘clusters’) with an increased stability, possibly due to a cooperative change in the microtubule lattice structure. The formation

Fig. 6 | Fchitax-3 promotes long, sheet-like microtubule defects and generates sites of tubulin incorporation. **a,b**, Cryo-EM images (representative of two experiments) of microtubules grown with $15 \mu\text{M}$ tubulin and 20 nM mCherry-EB3 without (**a**) or with (**b**) 100 nM Fchitax-3. Long, sheet-like defects are boxed. **c,d**, Quantification of percentage of total defects (**c**) and defects of certain length (**d**) in GMPCPP-stabilized, control (–Fchitax-3) ($n = 311$ microtubules) and Fchitax-3-treated microtubules (+Fchitax-3) ($n = 833$ microtubules), combined from two experiments each. **** $P < 0.0001$; NS, no statistically significant difference, $P = 0.2$, Pearson's χ^2 test. **e**, Top: time-lapse images illustrating that Fchitax-3 accumulation is accompanied by microtubule bending. Bottom left: an example of transverse microtubule tip fluctuations. Bottom right: average standard deviation (normalized to the values before Fchitax-3 accumulation) of the microtubule tip fluctuations before, during and after Fchitax-3 accumulation. $n = 11$, $N = 5$, ** $P = 0.0038$; NS, no statistically significant difference, $P = 0.55$, Mann–Whitney U -test. **f**, Left: kymographs illustrating microtubule dynamics with $15 \mu\text{M}$ tubulin, 20 nM GFP-EB3, 100 nM Fchitax-3 and 10 nM mCherry-CAMSAP3. Middle: scheme illustrating CAMSAP3 binding to a microtubule minus-end and protofilaments extending from a Fchitax-3 accumulation in the minus-end direction. Right: fluorescence intensity profiles and quantifications (mean \pm s.d.) showing CAMSAP3 intensity at the microtubule regions grown from the minus- (1) and plus-end (2) of the seed and Fchitax-3 accumulation (3). Data were normalized to the CAMSAP3 intensity of the microtubule grown from the minus-end (2). $n = 10$, $N = 3$ independent experiments. **g**, Left: kymographs showing FRAP within microtubule region with Fchitax-3 accumulation. White lightning bolt highlights the bleached region, and white arrowheads highlight tubulin fluorescence recovery within bleached area. Middle: fluorescence intensity profiles of unbleached and bleached microtubule regions with and without Fchitax-3 accumulation. Right: quantification (mean \pm s.d.) of tubulin fluorescence before, during and after photobleaching in control microtubules ($n = 14$) and microtubule regions with a Fchitax-3 accumulation ($n = 15$), $N = 3$ independent experiments. **** $P < 0.0001$, * $P = 0.1$, Mann–Whitney U -test. **h**, Quantification (mean \pm s.d.) of EB3 fluorescence at growing plus-ends or within microtubule regions with or without Fchitax-3 accumulation ($n = 30$ microtubules from $N = 3$ independent experiments). Intensity values were normalized to the intensity of EB3 at growing microtubule plus-ends. **** $P < 0.0001$, Mann–Whitney U -test. **i**, Model showing interaction of taxane-site ligands with microtubules. Taxanes show preference for GMPCPP- over GDP-bound microtubule lattice. The onset of catastrophe promotes taxane binding, possibly due to end tapering and the appearance of tubulin sheets. The drugs exhibit binding cooperativity and stabilize these microtubule structures. Subsequently, the regular microtubule structure is re-established due to tubulin incorporation; however, remnants of an incomplete microtubule structure with a high drug affinity remain; they stabilize the site, incorporate GTP-tubulin and promote repeated rescues.

of local clusters is reminiscent of polymorphic transitions in crystals, suggesting that the addition of a taxane-site ligand to dynamic microtubules induces altered forms of microtubule lattices.

The nucleotide state of tubulin plays a role in controlling taxane affinity for microtubules, with the GMPCPP-bound, extended

conformation being preferred over the compacted GDP or GTP γ S lattice, consistent with the data that both GMPCPP- and Taxol-bound microtubules have expanded lattice^{10,33,34}. However, the pattern of ligand binding to a growing microtubule cannot be explained by the nucleotide state of tubulin alone. Our data



suggest that taxane-site ligands can preferentially bind to incomplete microtubule structures present at the ends, and strongly modify the properties, of these structures (Fig. 6i). The increased affinity of taxanes for incomplete tubulin structures, such as tubulin sheets, can explain their binding kinetics: providing the tube is incomplete, taxane keeps binding, but if the sheet closes into a tube, a significant proportion of the drug molecules is released. Our data are consistent with the idea that, after tube closure and growth continuation, an open structure remains at the initial part of the drug accumulation zone, explaining why the drug can still exchange within this region and create a stable site that inhibits microtubule depolymerization. Incorporation of GTP-tubulin at the drug accumulation zones promotes their stability and their capacity to induce rescues, as described previously for other situations where microtubule lattice repair has been observed^{41–43}. Importantly, our data suggest that microtubule repair at drug accumulation sites is not complete—a part of the microtubule lattice remains open, but is not depolymerized due to the presence of drug molecules.

An interesting feature of taxane binding to microtubule lattices is its cooperative character. Our modelling based on the kinetic binding curves suggests that initially only a few tubulin dimers within the microtubule lattice can bind the drug, and that drug association catalyses the formation of additional binding sites in the vicinity. One potential explanation of such cooperativity could be based on the propagation of an extended conformational state of the microtubule lattice, which was observed for Taxol-bound microtubules by cryo-EM^{10,33,34} and in our X-ray fibre diffraction experiments. A similar elongation of the axial microtubule repeat has recently been proposed to underlie the positive cooperativity in the binding of kinesin-1 to microtubules⁴⁴. However, since taxane-site ligands can also affect lateral contacts between tubulin dimers^{13–16}, it is possible that alterations in these contacts account for propagating structural effects, such as a differential curvature of tubulin sheets.

Taxane-bound zones at microtubule ends represent suboptimal substrates for microtubule shrinkage, but also for microtubule growth. This leads to slow growth and frequent transitions between growth and shortening, which helps to explain the surprising observation that, although Taxol is a microtubule stabilizer, at low concentrations it perturbs microtubule growth in cells (reviewed in ref. 45; see ref. 22 for an example).

An important conclusion of our study is that the conformational transitions at microtubule ends, which lead to growth perturbation and catastrophes, also promote taxane-site ligand binding and microtubule stabilization by these compounds. One interesting consequence of this effect is that the distribution of ligand accumulations along the microtubule shaft reflects the history of the growth of this microtubule. Another important consequence is that taxane-site ligand binding to microtubules can be potentiated by low doses of catastrophe-inducing MTAs, and some evidence supporting this idea has already been reported based on cell culture experiments²³. Our data provide an explanation for this phenomenon and suggest that, in future work, it can be exploited for optimization of MTA-based cancer therapies.

Online content

Any methods, additional references, Nature Research reporting summaries, source data, extended data, supplementary information, acknowledgements, peer review information; details of author contributions and competing interests; and statements of data and code availability are available at <https://doi.org/10.1038/s41563-019-0546-6>.

Received: 2 February 2019; Accepted: 24 October 2019;







Published online: 09 December 2019

References

- Desai, A. & Mitchison, T. J. Microtubule polymerization dynamics. *Annu. Rev. Cell Dev. Biol.* **13**, 83–117 (1997).
- Cross, R. A. Microtubule lattice plasticity. *Curr. Opin. Cell Biol.* **19**, 451–463 (2018).
- Kueh, H. Y. & Mitchison, T. J. Structural plasticity in actin and tubulin polymer dynamics. *Science* **325**, 960–963 (2009).
- Brouhard, G. J. & Rice, L. M. Microtubule dynamics: an interplay of biochemistry and mechanics. *Nat. Rev. Mol. Cell Biol.* **19**, 451–463 (2018).
- Dumontet, C. & Jordan, M. A. Microtubule-binding agents: a dynamic field of cancer therapeutics. *Nat. Rev. Drug Discov.* **9**, 790–803 (2010).
- Yang, C. H. & Horwitz, S. B. Taxol((R)): the first microtubule stabilizing agent. *Int. J. Mol. Sci.* **18**, E1733 (2017).
- Steinmetz, M. O. & Prota, A. E. Microtubule-targeting agents: strategies to hijack the cytoskeleton. *Trends Cell Biol.* **28**, 776–792 (2018).
- Nogales, E. & Kellogg, E. H. Challenges and opportunities in the high-resolution cryo-EM visualization of microtubules and their binding partners. *Curr. Opin. Struct. Biol.* **46**, 65–70 (2017).
- Elie-Caille, C. et al. Straight GDP-tubulin protofilaments form in the presence of taxol. *Curr. Biol.* **17**, 1765–1770 (2007).
- Alushin, G. M. et al. High-resolution microtubule structures reveal the structural transitions in α -tubulin upon GTP hydrolysis. *Cell* **157**, 1117–1129 (2014).
- Zhang, R., Alushin, G. M., Brown, A. & Nogales, E. Mechanistic origin of microtubule dynamic instability and its modulation by EB proteins. *Cell* **162**, 849–859 (2015).
- Kellogg, E. H. et al. Near-atomic model of microtubule–tau interactions. *Science* **360**, 1242–1246 (2018).
- Prota, A. E. et al. Molecular mechanism of action of microtubule-stabilizing anticancer agents. *Science* **339**, 587–590 (2013).
- Prota, A. E. et al. Structural basis of microtubule stabilization by discodermolide. *ChemBiochem* **18**, 905–909 (2017).
- Wang, Y. et al. Mechanism of microtubule stabilization by taccalonolide AJ. *Nat. Commun.* **8**, 15787 (2017).
- Manka, S. W. & Moores, C. A. The role of tubulin–tubulin lattice contacts in the mechanism of microtubule dynamic instability. *Nat. Struct. Mol. Biol.* **25**, 607–615 (2018).
- Brown, T. et al. A phase I trial of taxol given by a 6-hour intravenous infusion. *J. Clin. Oncol.* **9**, 1261–1267 (1991).
- Weaver, B. A. How Taxol/paclitaxel kills cancer cells. *Mol. Biol. Cell* **25**, 2677–2681 (2014).
- Gianni, L. et al. Nonlinear pharmacokinetics and metabolism of paclitaxel and its pharmacokinetic/pharmacodynamic relationships in humans. *J. Clin. Oncol.* **13**, 180–190 (1995).
- Spratlin, J. & Sawyer, M. B. Pharmacogenetics of paclitaxel metabolism. *Crit. Rev. Oncol. Hematol.* **61**, 222–229 (2007).
- Mohan, R. et al. End-binding proteins sensitize microtubules to the action of microtubule-targeting agents. *Proc. Natl Acad. Sci. USA* **110**, 8900–8905 (2013).
- Bouchet, B. P. et al. Mesenchymal cell invasion requires cooperative regulation of persistent microtubule growth by SLAIN2 and CLASP1. *Dev. Cell* **39**, 708–723 (2016).
- Photiou, A., Shah, P., Leong, L. K., Moss, J. & Retsas, S. In vitro synergy of paclitaxel (Taxol) and vinorelbine (navelbine) against human melanoma cell lines. *Eur. J. Cancer* **33**, 463–470 (1997).
- Diaz, J. F., Strobel, R., Engelborghs, Y., Souto, A. A. & Andreu, J. M. Molecular recognition of Taxol by microtubules. Kinetics and thermodynamics of binding of fluorescent taxol derivatives to an exposed site. *J. Biol. Chem.* **275**, 26265–26276 (2000).
- Li, X., Barasoain, I., Matesanz, R., Diaz, J. F. & Fang, W. S. Synthesis and biological activities of high affinity taxane-based fluorescent probes. *Bioorg. Med. Chem. Lett.* **19**, 751–754 (2009).
- Bieling, P. et al. Reconstitution of a microtubule plus-end tracking system in vitro. *Nature* **450**, 1100–1105 (2007).
- Akhmanova, A. & Steinmetz, M. O. Control of microtubule organization and dynamics: two ends in the limelight. *Nat. Rev. Mol. Cell Biol.* **16**, 711–726 (2015).
- Duellberg, C., Cade, N. I., Holmes, D. & Surrey, T. The size of the EB cap determines instantaneous microtubule stability. *eLife* **5**, e13470 (2016).
- Montenegro Gouveia, S. et al. In vitro reconstitution of the functional interplay between MCAK and EB3 at microtubule plus ends. *Curr. Biol.* **20**, 1717–1722 (2010).
- Gigant, B. et al. Structural basis for the regulation of tubulin by vinblastine. *Nature* **435**, 519–522 (2005).
- Friel, C. T. & Welburn, J. P. Parts list for a microtubule depolymerising kinesin. *Biochem. Soc. Trans.* **46**, 1665–1672 (2018).
- Diaz, J. F., Barasoain, I. & Andreu, J. M. Fast kinetics of Taxol binding to microtubules. Effects of solution variables and microtubule-associated proteins. *J. Biol. Chem.* **278**, 8407–8419 (2003).

33. Zhang, R., LaFrance, B. & Nogales, E. Separating the effects of nucleotide and EB binding on microtubule structure. *Proc. Natl Acad. Sci. USA* **115**, E6191–E6200 (2018).
 34. Kellogg, E. H. et al. Insights into the distinct mechanisms of action of taxane and non-taxane microtubule stabilizers from cryo-EM structures. *J. Mol. Biol.* **429**, 633–646 (2017).
 35. Mitra, A. & Sept, D. Taxol allosterically alters the dynamics of the tubulin dimer and increases the flexibility of microtubules. *Biophys. J.* **95**, 3252–3258 (2008).
 36. Kikumoto, M., Kurachi, M., Tosa, V. & Tashiro, H. Flexural rigidity of individual microtubules measured by a buckling force with optical traps. *Biophys. J.* **90**, 1687–1696 (2006).
 37. Atherton, J. et al. A structural model for microtubule minus-end recognition and protection by CAMSAP proteins. *Nat. Struct. Mol. Biol.* **24**, 931–943 (2017).
 38. Jiang, K. et al. Microtubule minus-end stabilization by polymerization-driven CAMSAP deposition. *Dev. Cell* **28**, 295–309 (2014).
 39. Arnal, I. & Wade, R. H. How does Taxol stabilize microtubules? *Curr. Biol.* **5**, 900–908 (1995).
 40. Castle, B. T. et al. Mechanisms of kinetic stabilization by the drugs paclitaxel and vinblastine. *Mol. Biol. Cell* **28**, 1238–1257 (2017).
 41. Schaedel, L. et al. Microtubules self-repair in response to mechanical stress. *Nat. Mater.* **14**, 1156–1163 (2015).
 42. Aumeier, C. et al. Self-repair promotes microtubule rescue. *Nat. Cell Biol.* **18**, 1054–1064 (2016).
 43. Vemu, A. et al. Severing enzymes amplify microtubule arrays through lattice GTP-tubulin incorporation. *Science* **361**, eaau1504 (2018).
 44. Shima, T. et al. Kinesin-binding-triggered conformation switching of microtubules contributes to polarized transport. *J. Cell Biol.* **217**, 4164–4183 (2018).
 45. Jordan, M. A. & Wilson, L. Microtubules as a target for anticancer drugs. *Nat. Rev. Cancer* **4**, 253–265 (2004).
- Publisher's note** Springer Nature remains neutral with regard to jurisdictional claims in published maps and institutional affiliations.
- © The Author(s), under exclusive licence to Springer Nature Limited 2019

Lattice defects induced by microtubule-stabilizing agents exert a long-range effect on microtubule growth by promoting catastrophes

Ankit Rai^{a,1} , Tianyang Liu^b , Eugene A. Katrukha^a, Juan Estévez-Gallego^c, Szymon W. Manka^b , Ian Paterson^d , J. Fernando Díaz^c , Lukas C. Kapitein^a, Carolyn A. Moores^b, and Anna Akhmanova^{a,2} 

^aCell Biology, Neurobiology and Biophysics, Department of Biology, Faculty of Science, Utrecht University 3584 CH Utrecht, the Netherlands; ^bInstitute of Structural and Molecular Biology, Birkbeck, University of London, WC1E 7HX London, United Kingdom; ^cStructural and Chemical Biology, Centro de Investigaciones Biológicas Margarita Salas, Consejo Superior de Investigaciones Científicas 28040 Madrid, Spain; and ^dYusuf Hamied Department of Chemistry, University of Cambridge, Cambridge CB2 1EW, United Kingdom

Edited by Eva Nogales, University of California, Berkeley, CA; received July 11, 2021; accepted November 2, 2021

Microtubules are dynamic cytoskeletal polymers that spontaneously switch between phases of growth and shrinkage. The probability of transitioning from growth to shrinkage, termed catastrophe, increases with microtubule age, but the underlying mechanisms are poorly understood. Here, we set out to test whether microtubule lattice defects formed during polymerization can affect growth at the plus end. To generate microtubules with lattice defects, we used microtubule-stabilizing agents that promote formation of polymers with different protofilament numbers. By employing different agents during nucleation of stable microtubule seeds and the subsequent polymerization phase, we could reproducibly induce switches in protofilament number and induce stable lattice defects. Such drug-induced defects led to frequent catastrophes, which were not observed when microtubules were grown in the same conditions but without a protofilament number mismatch. Microtubule severing at the site of the defect was sufficient to suppress catastrophes. We conclude that structural defects within the microtubule lattice can exert effects that can propagate over long distances and affect the dynamic state of the microtubule end.

microtubule | Taxol | protofilament | in vitro reconstitution | photoablation

Microtubules are cytoskeletal polymers that rapidly switch between phases of growth and shortening, and this behavior, termed dynamic instability, plays a crucial role in the formation, maintenance, and reorganization of microtubule arrays during cell division, migration, and differentiation (1, 2). The transition from growth to shrinkage, an event called catastrophe, is known to occur when the protective cap of guanosine triphosphate (GTP)-bound tubulin subunits is reduced or lost, but the underlying mechanisms are still the subject of investigation (3, 4). One interesting property of microtubules is that the frequency of catastrophes depends on microtubule age: Microtubules that are growing for a longer time have a higher chance to switch to depolymerization (5, 6). Changes occurring at the microtubule end, such as loss of individual protofilaments or end tapering, have been shown to promote catastrophe (7–9). In principle, it is also possible that the catastrophe frequency at the plus end is affected by structural features in the microtubule lattice farther away from the tip, but this possibility has so far remained untested.

Structural studies have established that tubulin can form tubes with different protofilament numbers (10), dependent on the species, nucleation template, presence of different microtubule-associated proteins, and other properties of the polymerization reaction (e.g., ref. 11; reviewed in ref. 12). An important consequence of the structural plasticity of the microtubule lattice (13) is the formation of lattice defects, such as sites where a microtubule gains or loses one or more

protofilaments (11, 14–17). A recent cryoelectron tomography analysis showed that in some cell types, such as *Drosophila* neurons, variations and transitions in protofilament number are readily detectable (18) and are thus likely to be physiologically relevant. Switches in protofilament number can be introduced during microtubule growth, and their presence may affect microtubule dynamics in different ways. For example, defects can be repaired through tubulin incorporation, and the resulting islands of GTP-tubulin can trigger microtubule rescue (19–22). On the other hand, the presence of defects could potentially also induce catastrophes (as proposed in ref. 14), since conformational properties of the microtubule lattice might propagate over some distances (23).

To study the relationship between lattice defects and microtubule catastrophes, one should be able to directly correlate the presence of defects with the dynamics of microtubule ends. We recently found that fluorescent analogs of microtubule-stabilizing agents (MSAs) can be used to induce microtubule

Significance

Microtubules are major cytoskeletal filaments important for cell division, growth, and differentiation. Microtubules can rapidly switch between phases of growth and shortening, and this dynamic behavior is essential for shaping microtubule arrays. To obtain insights into mechanisms controlling microtubule dynamics, here we used microtubule-stabilizing agents such as Taxol and their fluorescent analogs to manipulate microtubule protofilament number and generate stable defects in microtubule lattices that can be visualized using fluorescence microscopy. We show that microtubule polymerization rate increases with protofilament number and that drug-induced microtubule lattice discontinuities can promote plus-end catastrophes at a distance of several micrometers. Our data indicate that structural defects in the microtubule wall can have long-range propagating effects on microtubule tip dynamics.

Author contributions: A.R. and A.A. designed research; A.R., T.L., J.E.-G., S.W.M., and J.F.D. performed research; I.P. contributed new reagents/analytic tools; A.R., T.L., E.A.K., J.E.-G., S.W.M., J.F.D., L.C.K., C.A.M., and A.A. analyzed data; and A.R., E.A.K., C.A.M., and A.A. wrote the paper.

The authors declare no competing interest.

This article is a PNAS Direct Submission.

This open access article is distributed under [Creative Commons Attribution License 4.0 \(CC BY\)](https://creativecommons.org/licenses/by/4.0/).

¹Present address: Department of Biochemistry, Faculty of Science, Banaras Hindu University, 221005 Varanasi, India.

²To whom correspondence may be addressed. Email: akhmanova@uu.nl.

This article contains supporting information online at <http://www.pnas.org/lookup/suppl/doi:10.1073/pnas.2112261118/-DCSupplemental>.

Published December 16, 2021.

lattice defects that can be visualized by fluorescence microscopy. When present at low concentrations, MSAs preferentially bind to microtubule plus ends that enter a “precatastrophe” state (24), which is manifested by the gradual loss of the GTP cap and reduced recruitment of end-binding (EB) proteins that detect GTP-bound microtubule lattice (25–27). Strong accumulation of MSAs at precatastrophe microtubule ends leads to the formation of stabilized patches of microtubule lattice, where the tube is incomplete and keeps incorporating GTP-tubulin but is not fully repaired (24). When microtubules switch to depolymerization, such persistent lattice defects, which coincide with the hotspots of MSA binding, can induce repeated rescues and, therefore, they were termed “stable rescue sites” (24).

Here, we used MSA-induced lattice defects to address two questions. First, what prevents complete repair of an MSA-induced persistent lattice defect? And second, does the presence of such a persistent defect affect the dynamics of the microtubule plus end? Since different MSAs are known to affect the number of protofilaments (15, 28–33), we hypothesized that persistent lattice defects could be associated with the changes in protofilament number and thus could not be fully repaired for geometrical reasons. We tested this idea by generating stable microtubule seeds with one MSA and then elongating them in the presence of another MSA, with the same or different preference for protofilament number. Use of fluorescent MSAs allowed us to directly follow drug binding. We found that precatastrophe microtubule ends accumulated MSAs in all conditions; however, the outcome of drug binding was different. When there was no mismatch in protofilament number between the seeds and the elongation conditions, drug accumulations were short in duration and length, and microtubule growth beyond such sites was processive. In contrast, when, based on the MSA properties, a mismatch in protofilament number could be expected, large and persistent drug accumulations were formed. The existence of such mismatches was confirmed by cryoelectron microscopy (cryo-EM) and by measuring microtubule growth rate, which became higher with increasing protofilament number. When microtubule ends extended beyond a mismatch-containing lattice defect, they displayed elevated catastrophe frequency. Laser-mediated severing of a microtubule at the site of the persistent defect reduced catastrophe frequency at the plus end. Our data demonstrate that local perturbations in microtubule structure can affect the state of the dynamic end at a distance of several micrometers.

Results

Protofilament Number Affects Microtubule Growth Rate. We first set out to test whether microtubules with different protofilament numbers display different dynamic properties. Protofilament number changes in response to the nucleotide bound to the regulatory E site or the presence of MSAs (15, 28–33). Therefore, to generate microtubules with different protofilament numbers, we prepared microtubule seeds with the slowly hydrolyzable GTP analog GMPCPP or with different microtubule-stabilizing drugs. Using X-ray fiber diffraction and cryo-EM, we confirmed previous observations showing that microtubule seeds generated in the presence of Taxol have predominantly 13 protofilaments (pf), whereas 14pf microtubules were observed in the presence of GMPCPP and docetaxel (Fig. 1 *A* and *B*) (15, 31–33). Microtubules stabilized with Alexa₄₈₈-epothilone B also had 14pf, whereas protofilament number shifted toward 15pf in the presence of discodermolide and 15/16pf with Fchitax-3 (Fig. 1 *A* and *B*). We next used these stabilized microtubule seeds to grow dynamic microtubules and observed their behavior using total internal reflection fluorescence (TIRF) microscopy as described previously (34, 35) (*SI Appendix, Fig. S1A*). In these assays, the seeds contained

rhodamine- and biotin-labeled tubulin for visualization and attachment to glass surface, respectively, and cryo-EM showed that in these conditions, Taxol-stabilized seeds predominantly contained 13pf, GMPCPP-stabilized seeds contained 14pf, and Fchitax-3-stabilized seeds contained 15/16pf (*SI Appendix, Fig. S1B*). Assays were performed either with tubulin alone or with the addition of mCherry-EB3, which serves as a microtubule plus-end marker and increases both the growth rate and catastrophe frequency in assays with purified tubulin (36) (Fig. 1 *C* and *SI Appendix, Fig. S1C*). In these assays, MSAs were used to prepare stable seeds but were not added during polymerization. Both with and without EB3, we found that microtubule growth rate increased with protofilament number (Fig. 1 *D, Upper* and *SI Appendix, Fig. S1D, Upper*). Calculation of the critical concentration C_c of microtubule polymerization and tubulin association rate constant k_{on} based on fitting of the dependence of the growth rate on tubulin concentration (37) indicated that C_c is lower and k_{on} is higher for microtubules with more protofilaments (Fig. 1 *E* and *SI Appendix, Fig. S1E*). Catastrophe frequency showed some variability between different conditions but was independent of protofilament number (Fig. 1 *D, Lower* and *SI Appendix, Fig. S1D, Lower*). As described previously (35), very few rescues were seen when microtubules were grown from GMPCPP seeds, while occasional rescues were found when drug-stabilized seeds were used, likely because some drug molecules could diffuse from the seeds and bind to the dynamic lattice.

Importantly, in these conditions, the nature of the drug present in the seeds had no effect on the polymerization rate—for example, all microtubules grown from 14pf seeds, including GMPCPP-stabilized ones, polymerized with the same speed. To further exclude that the observed differences in growth rates were caused by the drugs diffusing from the seeds, we labeled the seeds with different protofilament numbers in different colors and grew microtubules from two types of seeds on the same coverslip (*SI Appendix, Fig. S2A*). In these experiments, two types of seeds were exposed to exactly the same reaction mix, including the drugs that might be present in solution. Importantly, we observed that microtubules still displayed growth rates characteristic for their protofilament number (*SI Appendix, Fig. S2A*). For example, in the same reaction mix, microtubules grew from Taxol-stabilized seeds (13pf) slower than from GMPCPP (14pf) seeds (*SI Appendix, Fig. S2A*). We also investigated whether microtubule depolymerization rate depended on protofilament number but found no clear correlation: We observed that microtubules grown from 14pf or 15/16pf seeds depolymerized at the same rate, but slower than microtubules grown from Taxol-stabilized (13pf) seeds (*SI Appendix, Fig. S2B*). We conclude that when the growth conditions are the same, microtubule polymerization rate can be used to infer protofilament number.

Effects of MSAs on Microtubule Dynamics Depend on the Protofilament Number in the Seeds. Next, we investigated how microtubule dynamics would be affected by adding during polymerization an MSA with a protofilament number preference that was either the same (matching conditions) or different (mismatching conditions) from the one used during seed preparation (Fig. 24). Drug concentrations in the range 50 to 400 nM were used, because higher concentrations induced spontaneous microtubule nucleation, and we thus could not ensure that all observed microtubules grew from the preexisting seeds with the known protofilament number. We observed three types of dynamic microtubule behaviors. The first type of dynamics was semiprocessive growth interrupted by short (0.2- to 0.5- μ m) depolymerization events followed by rapid rescues (“semiprocessive growth”; Fig. 2 *B* and *C* and *SI Appendix, Fig. S3A* and *C*). The second type of dynamic behavior was manifested by frequent

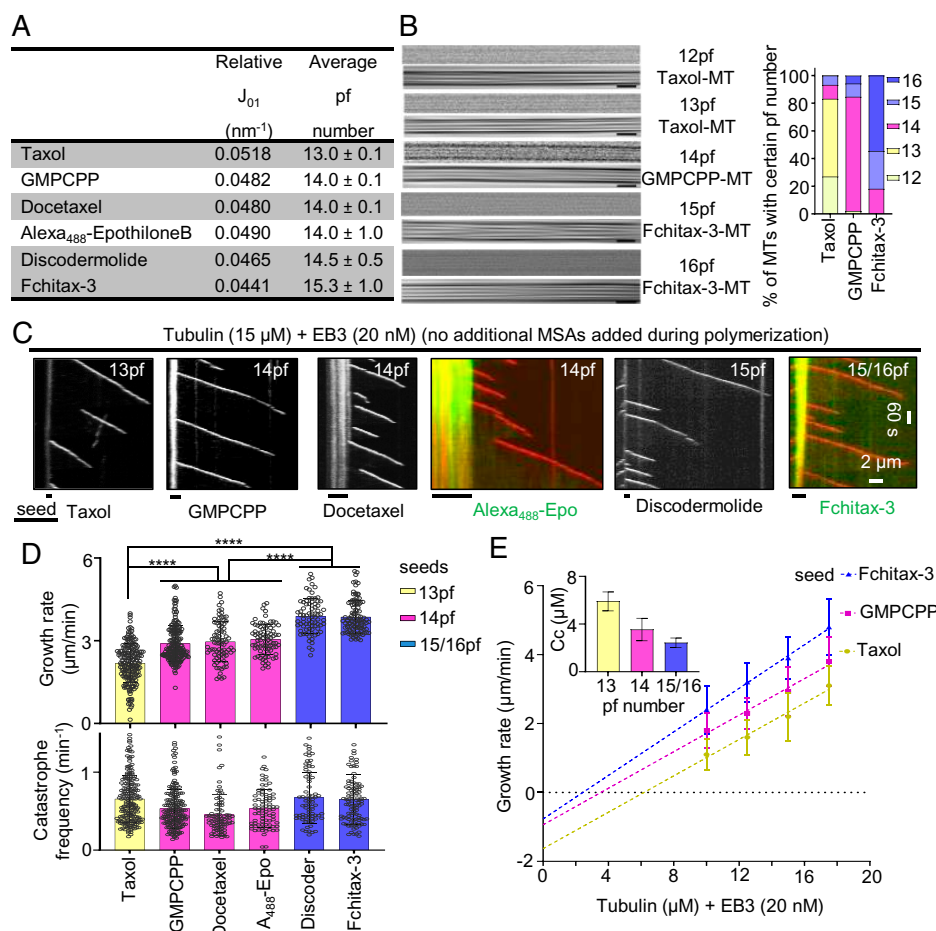


Fig. 1. Microtubule protofilament number affects microtubule growth rate. (A) X-ray fiber diffraction measurements for protofilament numbers of microtubules polymerized in the presence of different MSAs. For each condition, a total of 24 diffraction images were averaged and background-subtracted using ImageJ software. (B) Representative raw cryo-EM images and their filtered versions emphasizing their Moiré patterns. (Scale bars, 25 nm.) The bar graph shows microtubule (MT) protofilament number distribution determined by Moiré pattern visualization for each microtubule. Microtubule population: $n = 89$ for Taxol; $n = 52$ for GMPCPP; and $n = 77$ for Fchitax-3. (C) Representative kymographs showing microtubule dynamics in the presence of seeds stabilized with the indicated compounds, supplemented with tubulin (15 μM) and mCherry-EB3 (20 nM) in the absence of any additional MSAs during the reaction. (D) Quantification of growth rates (Upper) and catastrophe frequencies (Lower) in the presence of seeds with different protofilament numbers. From left to right, $n = 193$, 196, 82, 81, 76, and 104 growth events; $n = 2$ independent experiments for docetaxel, Alexa₄₈₈-epothilone B, and discodermolide; $n = 3$ independent experiments for Taxol, GMPCPP, and Fchitax-3. Error bars represent SD; **** $P < 0.0001$, Mann-Whitney U test. (E) Microtubule growth rate as a function of tubulin concentration (10 to 17.5 μM) from seeds with different protofilament numbers. Error bars represent SD; critical concentration C_c (mean \pm SEM), calculated based on the linear fits of the data, is shown (inset); $n = 3$ independent experiments. Microtubule growth events: $n = 280$, 161, and 221 for 10 μM ; $n = 369$, 254, and 193 for 12.5 μM ; $n = 193$, 196, and 104 for 15 μM ; and $n = 243$, 208, and 214 for 17.5 μM for Taxol, GMPCPP, and Fchitax-3, respectively.

catastrophes followed by long ($>0.5\text{-}\mu\text{m}$) depolymerization events and repeated rescues at the same site (stable rescue site, which will be termed here “SRS dynamics”; Fig. 2 *B* and *D* and *SI Appendix*, Fig. S3 *B* and *C*). The third type of dynamic behavior was characterized by catastrophes followed by long ($>0.5\text{-}\mu\text{m}$) depolymerization events and randomly distributed rescues (termed “random rescues”; Fig. 2*B* and *SI Appendix*, Fig. S4*A*). At 100 nM MSA concentrations, there was a clear difference in the occurrence of a particular type of dynamics, which depended on the combination of MSAs used for preparing the seeds and their elongation. When the protofilament number was expected to be the same (“matching conditions”; Fig. 2*A*), semiprocessive growth with very short depolymerization events strongly predominated (Fig. 2*B* and *C* and *SI Appendix*, Fig. S3*A* and *C*; short growth perturbations are highlighted by asterisks). In contrast, when the seeds were elongated in the presence of an MSA that had a protofilament number preference that was different from that of the MSA used for seed stabilization (“mismatching

conditions”; Fig. 2*A*), SRS dynamics (highlighted by white dashed lines) or random rescues (highlighted by yellow arrows) with long depolymerization events were observed (Fig. 2*B* and *D* and *SI Appendix*, Figs. S3*B* and *C* and S4*A*). When higher MSA concentrations were used during microtubule growth, random rescues were predominantly observed for mismatching conditions (*SI Appendix*, Fig. S4*A*), likely because rescues became more frequent, and depolymerization events were thus not long enough to reach the preceding stable rescue site. When MSA concentration was reduced, some microtubules displayed random rescues in matching conditions, because depolymerization events became longer but were typically still followed by rapid rescues (*SI Appendix*, Fig. S4*B*).

Importantly, microtubules grown in the presence of the same MSA showed very different dynamics depending on the seeds used. For example, microtubules grown in the presence of 100 nM Taxol displayed semiprocessive growth when extending from Taxol-stabilized seeds (13pf) but SRS dynamics or random

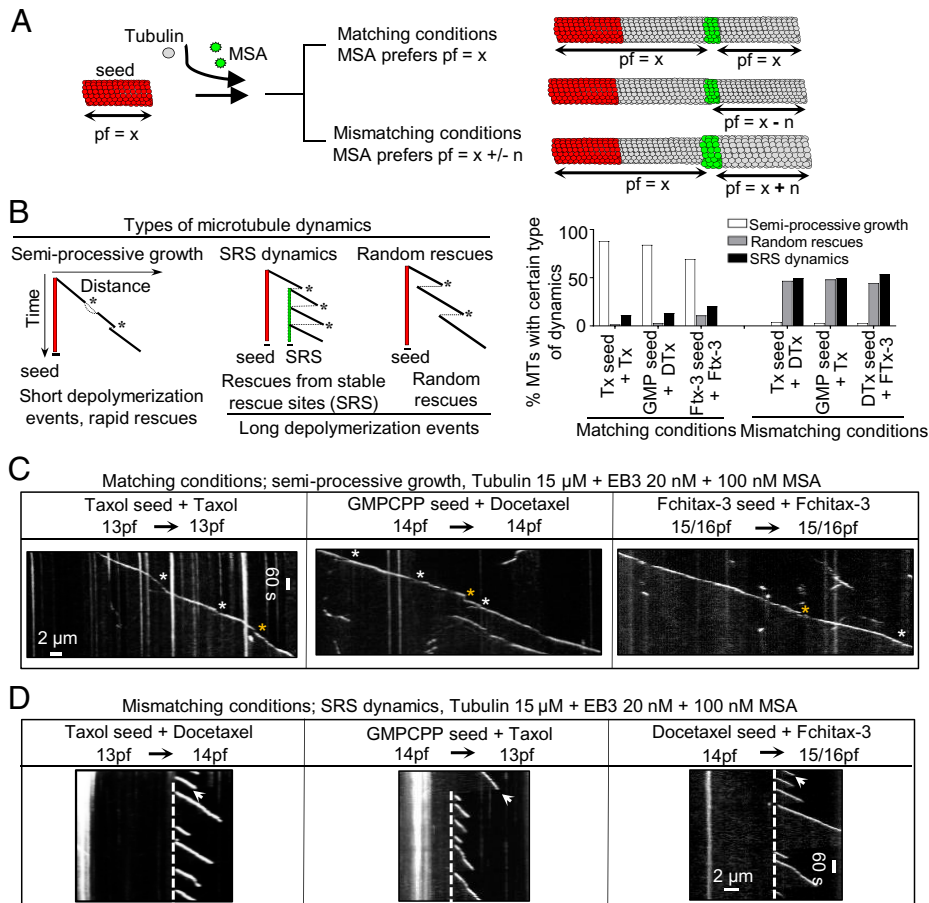


Fig. 2. Protofilament number mismatch between the seed and growth conditions affects microtubule dynamics. (A) A scheme illustrating microtubule growth from seeds in the presence of MSAs with the same or different protofilament number preference. MSA-binding zones are shown in green. (B, Left) A cartoon depicting kymographs corresponding to three types of microtubule dynamics observed in different conditions. Microtubule dynamics is defined as SRS dynamics if a microtubule regrows at least three times from the same site after undergoing catastrophes. A random rescue is a single rescue event after a depolymerization episode that is longer than 0.5 μm . Asterisks highlight catastrophe events in each condition. (B, Right) Quantification of microtubule dynamics observed in the indicated conditions; $n = 75$ microtubule seeds in all conditions; $n = 3$ independent experiments. (C and D) Representative kymographs showing microtubule dynamics in the indicated conditions. In matching conditions, short growth perturbation events followed by rapid rescues are highlighted (white asterisks highlight split comets and yellow asterisks highlight depolymerization events with length 0.2 to 0.5 μm). Stable rescue sites in mismatching conditions are highlighted by white stippled lines. A white arrow highlights a long depolymerization event ($>0.5 \mu\text{m}$); $n = 3$ independent experiments.

rescues when grown from GMPCPP-stabilized (14pf) or Fchitax-3-stabilized (15/16pf) seeds (Fig. 2 B–D and SI Appendix, Fig. S3). In contrast, in the presence of docetaxel, microtubules grew semiprocessively from GMPCPP or docetaxel-stabilized (14pf) seeds but showed SRS dynamics or random rescues when grown from Taxol- or Fchitax-3-stabilized seeds (Fig. 2 B–D and SI Appendix, Fig. S3). Similar results were also obtained when microtubules were grown without mCherry-EB3, although the absence of a plus-end marker made the detection of short depolymerization events less reliable (SI Appendix, Fig. S5). For subsequent analyses, we therefore focused on the data obtained with MSA concentrations of 100 nM in the presence of 20 nM mCherry-EB3. Together, these results demonstrate that the (mis)match between the protofilament number of the seed and the number preferred by the MSA present during elongation has a strong effect on microtubule growth dynamics, even when the microtubule tip is far away from the seed.

Larger and More Persistent Drug Accumulations Are Observed in Mismatching Conditions. To better understand the origin of the striking differences in the observed microtubule dynamics in matching and mismatching conditions, we visualized drug

binding using fluorescent drug analogs. Stable rescue sites coincide with the formation of drug accumulation hotspots, which initiate directly behind a growing microtubule plus end entering a precatastrophe state that can be distinguished by the reduction in EB3 signal (24) (Fig. 3 A and B). Microtubule lattice zones with high drug affinity can extend for several micrometers but then abruptly stop (Fig. 3 A and B), and previous work suggested that they might represent incomplete tubes, which stop binding the drug when they close (24).

In mismatching conditions, such as GMPCPP seeds (14pf) elongated in the presence of Fchitax-3 (15/16pf) or Taxol-stabilized seeds (13pf) elongated in the presence of Alexa₄₈₈-epothilone B (14pf), we observed large and persistent drug accumulation zones that coincided with stable rescue sites (Fig. 3 A and B). In contrast, in matching conditions (GMPCPP-stabilized seeds elongated in the presence of Alexa₄₈₈-epothilone B [14pf] or Fchitax-3-stabilized seeds elongated in the presence of Fchitax-3 [15/16pf]), drug accumulation patches were short in duration and length (Fig. 3 C–E and SI Appendix, Fig. S6A). In both conditions, drug binding always initiated directly behind a microtubule plus end after it started to lose mCherry-EB3 signal, indicating a growth perturbation. The kinetics of the reduction of EB3 signal before drug binding showed considerable

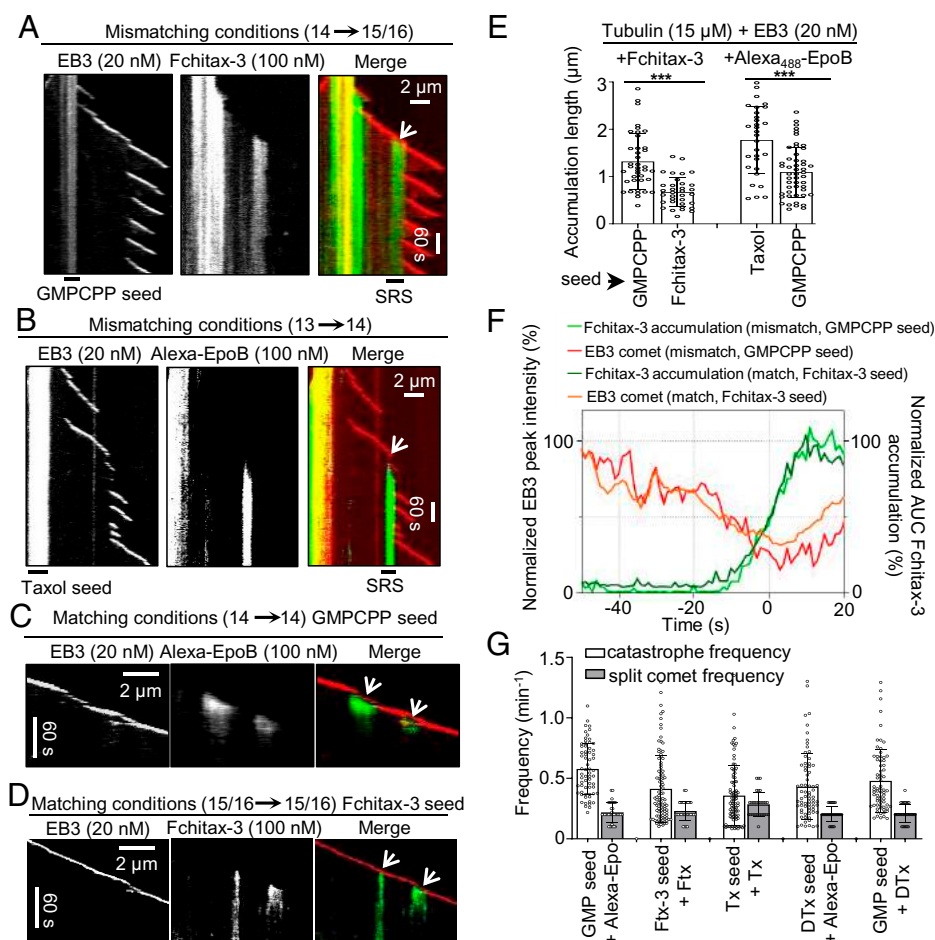


Fig. 3. Extent of MSA accumulation at precatastrophe microtubule tips depends on the match between the seed and growth conditions. (A and B) Representative kymographs illustrating drug accumulations in mismatching conditions. Microtubules were grown from GMPCPP seeds (A) or Taxol seeds (B) in the presence of 15 μ M tubulin and 20 nM mCherry-EB3 with Fchitax-3 (100 nM) (A) or Alexa₄₈₈-epothilone B (100 nM) (B). White arrows indicate stable rescue sites with drug accumulations. (C and D) Representative kymographs illustrating drug accumulations in matching conditions. Microtubules were grown from GMPCPP seeds (C) or Fchitax-3 seeds (D) in the presence of 15 μ M tubulin and 20 nM mCherry-EB3 with Alexa₄₈₈-epothilone B (100 nM) (C) or Fchitax-3 (100 nM) (D). Split comets are indicated with white arrows. (E) Quantification of drug accumulation lengths in the indicated conditions. Error bars represent SD; from left to right, $n = 39, 34, 30,$ and 50 ; $n = 3$ independent experiments; $***P < 0.001$. (F) Time plot of averaged normalized maximum intensity of fitted EB3 comet (orange and red) and normalized area under the curve (AUC) of fitted Fchitax-3 (light and dark green) intensity profiles in mismatching conditions (as shown in A; $n = 9$ kymographs from five experiments) and in matching conditions (as shown in D; $n = 38$ kymographs from five experiments). Individual curves were aligned by maximizing cross-correlation between Fchitax-3 time curves. Error bars represent SEM. (G) Frequencies of catastrophes (calculated as the frequency of all growth perturbations including split comet events) and split comet events in different matching conditions. From left to right, $n = 65, 100, 91, 71,$ and 70 for catastrophe frequencies for the indicated conditions and $n = 60, 66, 73, 62,$ and 63 catching-up events from 30 microtubules for split comet frequencies; $n = 3$ independent experiments. Error bars represent SD.

variability but was similar in matching and mismatching conditions (Fig. 3F), indicating that in both situations, microtubules could enter a precatastrophe state. The initial phase of drug accumulation was also very similar for matching and mismatching conditions (Fig. 3F).

Importantly, growth perturbations in matching conditions were typically of limited duration and were often accompanied by the emergence of a second, faster comet at the rear of the drug accumulation site (Fig. 3 C and D and *SI Appendix, Fig. S64*). Previous work showed that a “catching-up” comet appears when some protofilaments at the growing microtubule tip are stalled whereas the others keep elongating. When the stalled protofilaments start to regrow, a faster rear comet emerges and ultimately fuses with the leading one (8, 38). We observed split comets during growth perturbations in all tested matching conditions, and also when nonfluorescent MSAs were used (*SI Appendix, Fig. S6 B and C*). Clear split comets were seen in 38 to 79% of all catastrophe events detected in

matching conditions (Fig. 3G; all growth perturbations with length $>0.2 \mu$ m, including split comet events, were considered as catastrophes, as indicated by asterisks in Fig. 2B). Since the two comets must be located at a significant distance from each other to be registered as a “split comet” by fluorescence microscopy, these numbers are likely underestimates of the actual frequency of such events. We conclude that in matching conditions, growth perturbations are followed by the formation of catching-up comets, which likely help to restore a normally growing microtubule plus end, leading to semiprocessive microtubule growth.

In mismatching conditions, drug accumulation zones were longer and much more persistent (Fig. 3 A–E). The binding density of Fchitax-3 in mismatching conditions [approximately one or two drug molecules per 8 nm (24)] was higher than in matching conditions (0.3 to 0.9 molecules per 8-nm microtubule length; *SI Appendix, Fig. S6D*). This can be explained by the fact that in mismatching conditions, drug accumulations

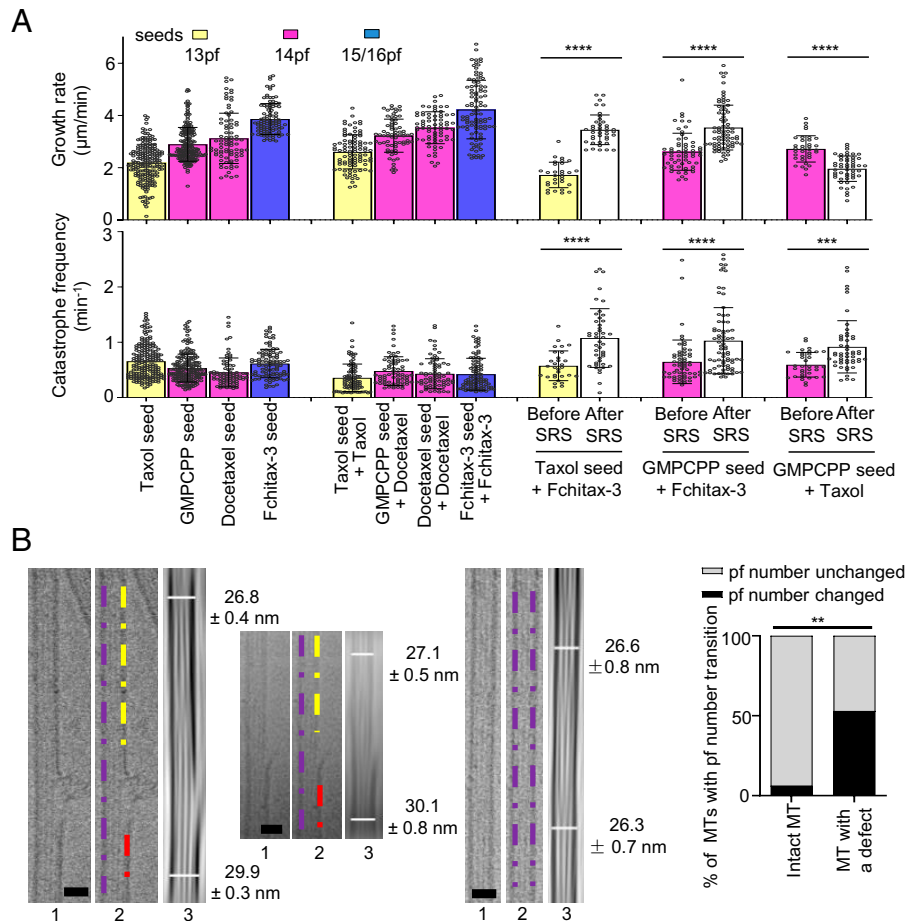


Fig. 4. Lattice defects observed in mismatching conditions are associated with switching of protofilament number. (A) Quantification of growth rates (Upper) and catastrophe frequencies (Lower; calculated as the frequency of all growth perturbations including catching-up events) for the indicated conditions. For better comparison, data from Fig. 1D are presented again in the present panels; $n = 193, 196, 82$, and 104 microtubule growth events for microtubules polymerized from Taxol, GMPCPP, docetaxel, and Fchitax-3 seeds; $n = 91, 70, 71$, and 100 in the presence of Taxol seed + Taxol (100 nM), GMPCPP seed + docetaxel (100 nM), docetaxel seed + docetaxel (100 nM), and Fchitax-3 seed + Fchitax-3 (100 nM); $n = 30$ and 40 for Taxol seed + Fchitax-3 (100 nM) before and after SRS formation; $n = 60$ and 75 for GMPCPP seed + Fchitax-3 (100 nM) before and after SRS formation; $n = 35$ and 51 for GMPCPP seed + Taxol (100 nM) before and after SRS formation; $n = 3$ independent experiments. Error bars represent SD. The colors of the bars and protofilament values indicate the protofilament number preferences of a particular drug used. **** $P < 0.001$, **** $P < 0.0001$, Mann-Whitney U test. (B) Representative raw cryo-EM images and their filtered versions with enhanced microtubule Moiré patterns showing the diameter difference (protofilament number transition) for microtubules grown from GMPCPP seeds in the presence of Fchitax-3 (mismatching condition; Fig. 3A). For each panel, Left and Central show defect-containing microtubules and Right shows a microtubule with no visible defects. (Scale bars, 25 nm.) Images 1 and 2 are raw cryo-EM images, with purple, yellow, and red dashed lines highlighting diameter differences on either side of a defect in image 2. Image 3 shows the diameters for two ends of a microtubule. Diameters were measured in Fiji. Percentage of microtubules with protofilament number transition in microtubules with no visible defects ($n = 19$) and microtubules with sheet-like defects ($n = 17$). The percentage differences were evaluated by two-sided Fisher's exact test; ** $P = 0.0023$.

expand for a longer time, possibly because a normal tube is more difficult to restore and protofilaments continue growing as a sheet or some other microtubule end structure that promotes drug binding. Thus, a mismatch between the protofilament number preference of the MSA used to prepare the seeds and to elongate them inhibits the restoration of a growing microtubule plus end after a growth perturbation has occurred and a drug accumulation has formed.

Lattice Defects Observed in Mismatching Conditions Are Associated with Switching of Protofilament Number. We hypothesized that binding of the drug to a precatastrophe microtubule tip either induces or stabilizes tubes with a protofilament number fitting with the specific preference of the drug used. In mismatching conditions, this would cause a protofilament number switch occurring at the stable rescue site, and this could explain why such sites do not get fully repaired. If this hypothesis is correct,

a microtubule will be expected to grow with the speed characteristic for the number of protofilaments present in the seed before the stable rescue site, but with a speed characteristic for the MSA present in the growth reaction after it. We found that in matching conditions, the addition of any MSA caused an increase in microtubule growth rate, but the correlation between the rate and protofilament number was retained (Fig. 4A, Upper). Interestingly, microtubules with SRS dynamics in mismatching conditions displayed growth rates characteristic for the seed before the rescue site and the growth rate matching better that of the MSA used in the growth reaction after the stable rescue site. For example, when GMPCPP seeds (14pf) were elongated in the presence of Fchitax-3 (15/16pf) or Taxol (13pf), the growth rate was characteristic for 14pf microtubules before the stable rescue site but was elevated after a stable rescue site in the presence of Fchitax-3 and decreased in the presence of Taxol (Fig. 4A, Upper). In contrast, in matching conditions, growth

rate before and after a growth perturbation did not change (*SI Appendix, Fig. S7A*). It should be noted, however, that the changes in growth rate did not completely match the speeds of microtubule growth when the same MSA was used for seed stabilization and elongation (Fig. 4 *A, Upper*). This likely reflects variability in protofilament number after the switch at a stable rescue site.

Further support for the occurrence of protofilament number switching at the stable rescue sites was obtained by cryo-EM. In our previous study (24), we found that microtubule lattice discontinuities corresponding to Fchitax-3 accumulations can be detected by cryo-EM. Here, we analyzed these data focusing on the microtubule diameter at the two sides of a lattice defect and found that protofilament number changed in ~53% of such cases, whereas in microtubules lacking defects switches in protofilament number were rare (Fig. 4*B* and *SI Appendix, Fig. S7B*). Since not all defects detected by cryo-EM might represent stable rescue sites observed by fluorescence microscopy, this number likely represents an underestimate of the actual switching of protofilament number at stable rescue sites. Thus, MSAs present during microtubule elongation can induce a switch to their preferred protofilament number at the stable rescue site.

Protofilament Number Mismatch between the Seed and the Growing Microtubule Lattice Promotes Catastrophes. Having established that stable rescue sites can correspond to regions where a switch in protofilament number takes place, we next asked how such sites affect growth of microtubules extending beyond them. Interestingly, we found that whereas catastrophe frequency (calculated as the frequency of all growth perturbations >0.2 μm including catching-up events) remained constant for microtubules growing in matching conditions, it was strongly increased for the growth events occurring after the stable rescue site (Fig. 4 *A, Lower*). The increase in catastrophe frequency was similar for microtubules that switched to higher (e.g., from 13pf or 14pf to 15/16pf) or lower (from 14pf to 13pf) numbers of protofilaments (Fig. 4 *A, Lower*). This observation was surprising, because one would expect that after switching to the protofilament number “preferred” by the MSA present in solution, a microtubule will be further growing in matching conditions and should thus display semiprocessive growth without long depolymerization events. However, this was not the case: Microtubule plus ends entering a precatastrophe state after a stable rescue site typically did not accumulate MSAs and simply switched to depolymerization, which proceeded all the way back to the preceding stable rescue site (Fig. 3 *A* and *B*). Whereas 48% of all catastrophe and precatastrophe events (distinguished by strong reduction or complete loss of the EB3 signal) occurring during microtubule outgrowth from the seed led to drug accumulation and formation of a stable rescue site, only 5% of such events occurring after a stable rescue site triggered drug accumulation and microtubule stabilization (*SI Appendix, Fig. S8A*). Formation of a secondary stable rescue site was thus quite rare: For example, when microtubules extended from GMPCPP-stabilized seeds in the presence of Fchitax-3, the formation of secondary stable rescue sites was seen only in 11% of all observed microtubules (*SI Appendix, Fig. S8B*). This suggests that some properties of a precatastrophe microtubule plus end extending after a stable rescue site (after a microtubule has incorporated a lattice defect) are different from those of microtubule ends growing directly from the seed.

To explore the underlying mechanism, we analyzed the intensities of EB3 comets and microtubule tip tapering during growth episodes from the GMPCPP-stabilized seed (14pf) either in the absence of drugs (control) or after a stable rescue site induced by discodermolide (14/15pf, mismatching

conditions). We note that Fchitax-3 or Alexa₄₈₈-epothilone B could not be used in these experiments because we used green (HiLyte 488-labeled tubulin) fluorescence to obtain tubulin profiles. We focused on the 40-s time interval preceding a catastrophe in order to determine whether the precatastrophe plus ends of microtubules growing directly from the seed or from a stable rescue site are somehow different. Microtubule end tapering was similar in both conditions (*SI Appendix, Fig. S8C*). The reduction of EB3 signal during catastrophe onset, which is expected to reflect the kinetics of GTP cap loss during catastrophe initiation, was also quite similar, although the curve was somewhat less steep for microtubules growing from seeds compared with microtubules elongating beyond a stable rescue site (*SI Appendix, Fig. S8D*). A higher-resolution analysis would be needed to determine what makes precatastrophe microtubule tips growing from seed different from those elongating after a stable rescue site.

Microtubule Severing at the Lattice Defect Site Suppresses Catastrophes. Why do microtubules growing beyond a stable rescue site display more catastrophes? One possibility is that a lattice defect with a different number of protofilaments on the two sides affects the growth at the plus end through a long-range conformational alteration or mechanical strain. If this is the case, severing the microtubule at the site of the defect should reduce catastrophe frequency. To test this idea, we performed microtubule severing on a TIRF microscope using a pulsed 532-nm laser and observed the dynamics of the severed part of the microtubule (*SI Appendix, Fig. S9A*). The severed microtubule fragment was no longer attached to the coverslip. However, due to the presence of methylcellulose, which increases the viscosity of the solution and dampens fluctuations, most severed microtubule fragments did not float away but stayed close to the surface and could still be observed by TIRF microscopy (*SI Appendix, Fig. S9B* and *Video S1*). In some cases, they underwent diffusive movements; however, movements of the whole microtubule segment could be easily distinguished from microtubule growth and shortening by the synchronous displacement of fluorescent speckles present along the microtubule shaft (*SI Appendix, Fig. S9B*). After microtubule severing in the absence of MSAs (microtubules polymerized in the presence of GMPCPP seeds with 15 μM tubulin and 20 nM EB3), freshly generated microtubule plus ends typically depolymerized, whereas freshly generated minus ends displayed heterogeneous behavior. The poor survival of microtubules after severing and the heterogeneity in minus-end dynamics precluded a meaningful analysis of the severing data in the absence of MSAs.

In the presence of an MSA such as Fchitax-3, the severed microtubule ends were typically quite stable. To generate microtubules with defects that would be visible by fluorescence microscopy, we grew microtubules in mismatching conditions from GMPCPP-stabilized seeds (14pf) in the presence of 100 nM Fchitax-3 (15/16pf), rhodamine-labeled tubulin, and 20 nM mCherry-EB3. After photoablation, the newly generated plus end, which remained attached to the seed, as well as the new minus end and the preexisting plus end of the microtubule fragment that was detached from the seed, could all polymerize (Fig. 5*A*). Imaging before photoablation and the photoablation itself induced significant photobleaching, and the tubulin freshly incorporated at the growing microtubule ends after severing could be readily observed because its signal was brighter; growing plus ends were additionally visualized by the accumulation of mCherry-EB3, that was detected in the same fluorescent channel as tubulin (Fig. 5*A*). Even when the severed end underwent some displacement after photoablation, the plus and the minus ends could be easily distinguished from each other by their growth rate, and the remnant of the drug

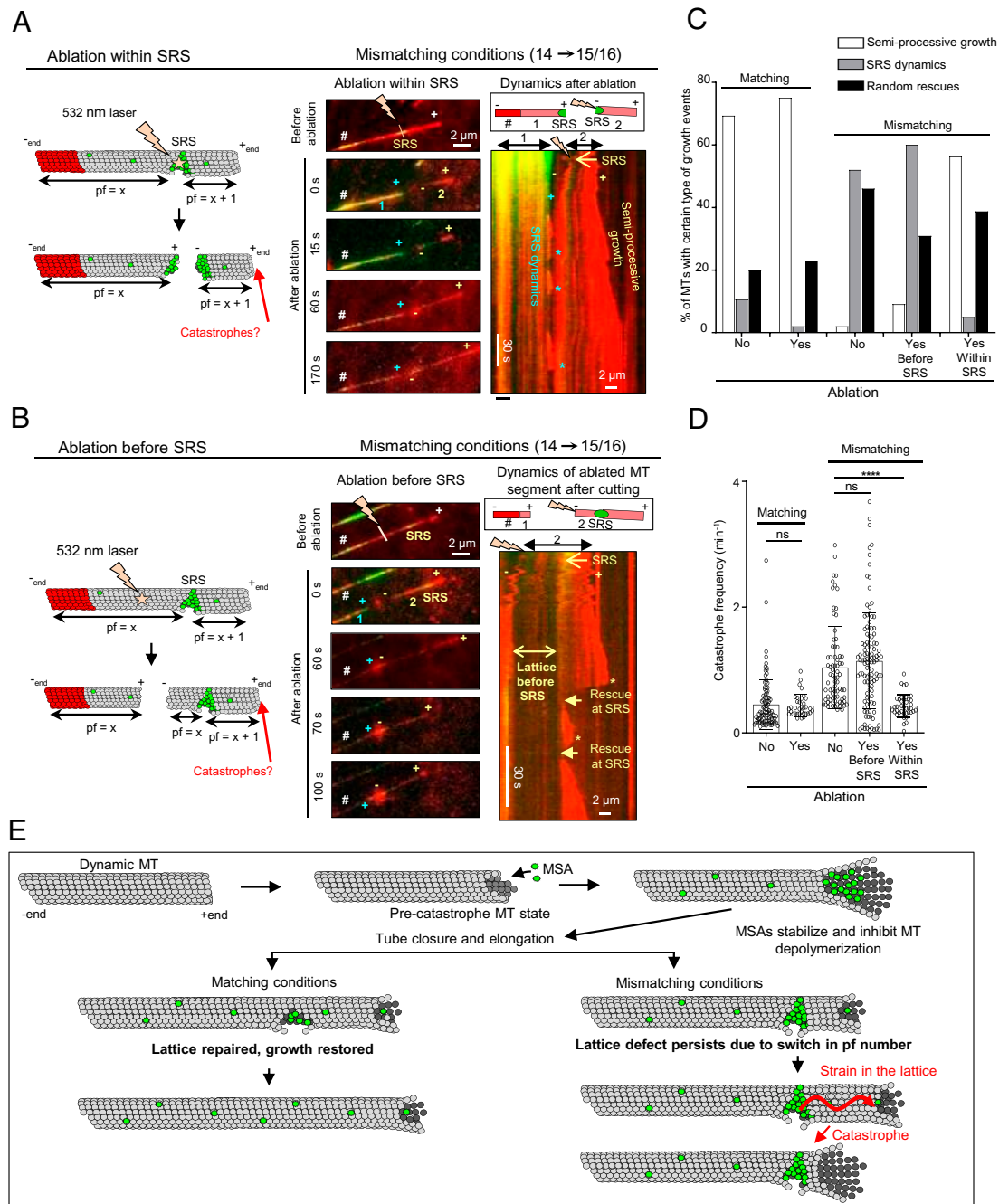


Fig. 5. Microtubule severing at the stable rescue site suppresses catastrophes. (A and B) Schematic representation and still images showing photoablation of microtubule regions within (A) or before (B) a drug accumulation zone (SRS) and kymographs showing microtubule dynamics of the severed parts. The assay was performed in the presence of GMPCPP seeds with 15 μ M tubulin supplemented with 3% rhodamine-tubulin, 20 nM mCherry-EB3, and 100 nM Fchitax-3. The time-lapse images before photoablation show the presence of stable rescue sites; the site of ablation within (A) and before (B) the stable rescue site is indicated by a lightning bolt. The newly generated microtubule fragments (1: seed-attached part; 2: the part that is detached from the seed after ablation), microtubule plus (+) ends, and the new plus (+) and minus (–) ends generated after ablation are indicated. In time-lapse images, # indicates the position of the GMPCPP seed. (A) The kymograph illustrates the dynamics of both fragments (1 and 2, as shown in the scheme) generated after ablation. (B) The kymograph illustrates the dynamics of the severed microtubule fragment (2, as shown in the scheme). Asterisks highlight catastrophes, and rescues at the stable rescue site are indicated by arrows in B. The labels are in blue for fragment 1 (seed-attached microtubule part) and yellow for fragment 2 (the part detached after ablation); $n = 5$ independent experiments. (C) Quantification of growth dynamics of the unsevered and severed microtubule segment in matching ($n = 75$, no severing; $n = 35$, after severing) and mismatching conditions; $n = 100$, 60, and 55 for no ablation, or ablation either before or within a drug accumulation area, respectively. (D) Quantification of catastrophe frequencies (calculated as the frequency of all growth perturbations including catching-up events). Matching conditions (Fchitax-3 seeds + 100 nM Fchitax-3): $n = 100$ (no ablation) and $n = 35$ (after ablation). Mismatching conditions (GMPCPP seeds + 100 nM Fchitax-3): $n = 76$ (no ablation, after the formation of a stable rescue site), $n = 115$ (after photoablation in a region preceding the Fchitax-3 accumulation area [SRS]), and $n = 39$ (after photoablation within SRS). ns, not significant; **** $P < 0.0001$, Mann–Whitney U test. (E) Model depicting microtubule lattice repair in matching and mismatching conditions. In the precatastrophe state, MSAs stabilize depolymerizing protofilaments and inhibit depolymerization. In matching conditions, this leads to rapid repair of microtubule defects and restoration of microtubule growth. In mismatching conditions, lattice defects persist despite repair due to a switch in protofilament number. The presence of a defect might generate strain in the lattice, which would affect the growing microtubule end and induce catastrophe.

accumulation zone at the stable rescue site was also visible (labeled as SRS in Fig. 5A).

When we severed microtubules directly at the site of Fchitax-3 accumulation (a stable rescue site), a part of the drug accumulation zone at the seed-attached microtubule fragment was often preserved after ablation. The plus end outgrowing from this zone displayed frequent catastrophes, typical for the SRS dynamics (blue asterisks in Fig. 5A and *SI Appendix, Fig. S104*). However, the catastrophe frequency at the plus end of the newly generated microtubule fragment distal from the seed (with the minus end located at the former stable rescue site) significantly decreased and a large proportion of microtubules switched from SRS dynamics with long depolymerization episodes to semiprocessive growth with short depolymerization episodes (Fig. 5A, C, and D, *SI Appendix, Fig. S104*, and *Video S2*).

In contrast, when we severed microtubules at a location preceding an Fchitax-3 accumulation zone, so that the stable rescue site with the flanking region on the minus-end side was preserved, microtubule plus ends distal from the severing site still underwent catastrophes, as was typical for the SRS dynamics (Fig. 5B–D, *SI Appendix, Fig. S10B*, and *Video S3*). Further, in matching conditions, we did not observe any difference in microtubule growth pattern before and after ablation: When ablated within or before drug accumulation zones, both newly generated microtubule plus ends exhibited semiprocessive growth (Fig. 5C and D and *SI Appendix, Fig. S11A*).

These data support the idea that drug-induced lattice discontinuities can exert an effect on the growth of microtubule plus ends located a significant distance away. To estimate this distance, we measured the average length of microtubule growth from the stable rescue site. This length was shorter than the average microtubule growth length after a seed, in line with the conclusion that catastrophe frequency after a stable rescue site is elevated (*SI Appendix, Fig. S11B*). However, microtubules could still extend from a stable rescue site for 1 to 10 μm before undergoing a catastrophe (*SI Appendix, Fig. S11B*). This indicates that conformational alterations or strain can propagate from a drug-induced defect to induce plus-end catastrophe at a distance encompassing hundreds of tubulin dimers.

Discussion

In this study, we addressed how microtubule lattice defects induced by MSAs affect growth at the microtubule plus end. We made use of the fact that when microtubules are grown in the presence of nonsaturating concentrations of MSAs, such as taxanes, the drugs strongly bind to microtubule ends in a precatastrophe state and thereby induce regions of increased microtubule stability, termed stable rescue sites (24). Importantly, these sites can contain “holes” in the microtubule wall, where fresh tubulin can be incorporated (24). The exact structural nature of these defects is likely to be complex. For example, recent cryo-EM work has shown that microtubules are not perfectly cylindrical but display strong local deviations from helical symmetry with different lateral contact geometries, and these deviations can be affected by taxanes (39). Local deviations from a cylindrical shape and additional types of microtubule lattice conformations, such as tubulin sheets (40) or protofilament flares (41), will likely have a major impact on the defect structure, stability, and affinity for MSAs. Importantly, in the current study, we show that MSA-induced lattice defects represent areas of alterations in protofilament number, providing a simple geometrical reason for their persistence over time, despite continuous microtubule repair. This view is supported both by cryo-EM data and by measuring microtubule growth speeds, which we found to correlate with protofilament number.

The observation that an increase in microtubule protofilament number leads to a higher growth rate in the absence of a clear effect on the catastrophe frequency or depolymerization rate is unexpected and intriguing. In principle, one might expect that if the flux of tubulin subunits onto the end were independent of protofilament number, more protofilaments would lead to slower growth. Since we find that microtubules with more protofilaments grow faster, tubulin flux is probably not a major determinant of the microtubule growth rate in the conditions we use. Microtubules with higher protofilament number have a smaller angular separation between protofilaments, and this can affect the strength of lateral tubulin bonds and the ease with which they form. The current understanding of the molecular details of microtubule growth relies on combining experiments with modeling (42–47). For example, one recent model of microtubule polymerization assumes that growing microtubule tips have flared protofilaments, to the end of which tubulin dimers are added before the protofilaments associate with each other laterally (48). In this model, lateral interactions between tubulins were described by two parameters, an activation energy barrier and bond strength. Increasing protofilament number could reduce the lateral activation energy barrier and lead to stronger lateral bonds. According to this model, both effects would accelerate microtubule growth; however, these effects might potentially compensate each other during depolymerization, because strengthening of the lateral bonds would impede microtubule disassembly, whereas reducing the lateral activation energy barrier could promote it (48). Furthermore, the abundance of various types of lateral tubulin contacts, such as “seam-like” contacts between α - and β -tubulin, which may be weaker and potentially unfavorable for microtubule growth, can be different in microtubules with different protofilament number and can be affected by MSAs (10, 11, 39, 49, 50). Four-start microtubule lattices (15/16pf), which have no seam, may therefore grow faster. Finally, if microtubules initially grow as two-dimensional tubulin sheets (40), sheet closure might occur more readily for microtubules with more protofilaments.

Modification of protofilament number using MSAs allowed us to reproducibly generate lattice defects and explore the consequences they have for microtubule dynamics (Fig. 5E). Strikingly, we found that although a microtubule could polymerize beyond a persistent lattice defect for lengths up to several micrometers, microtubule plus-end dynamics were affected, as the catastrophe frequency after the defect was significantly increased (Fig. 5E). A striking difference between microtubule plus ends grown from defect-bearing stable rescue sites and from stabilized seeds was that the latter could be efficiently “rescued” by an MSA once they entered a precatastrophe state. Drug accumulations leading to microtubule stabilization were ~ 10 -fold more frequent at the precatastrophe tips growing from seeds compared with microtubule ends entering a catastrophe after a preceding stable rescue site. These data indicate that some conformational aspects of a precatastrophe plus end during growth after a seed are different from those of a plus end elongating beyond a stable rescue site, and this might reflect differences in the catastrophe induction mechanism. However, our fluorescence-based measurements detected no significant change in microtubule end tapering and only a slight difference in the decay in EB3 intensity at precatastrophe ends of microtubules growing from seeds or after a stable rescue site. It would be interesting to use cryoelectron tomography to analyze the differences between growing microtubule ends in these conditions.

Strikingly, when microtubules were growing in matching conditions (when the MSAs used to stabilize the seeds and to elongate them had the same protofilament number preference), almost every growth perturbation resulted in rapid drug

binding and tip repair, leading to semiprocessive microtubule growth. These data show that the state and dynamics of the microtubule plus end depend not just on the conditions of polymerization but also on the state of the preceding lattice (Fig. 5E). For example, microtubules growing in the presence of 100 nM Fchitax-3 from an Fchitax-3-stabilized seed and from a GMPCPP-stabilized seed after a stable rescue site encounter exactly the same concentrations of the drug and tubulin. Yet, in the first case, microtubule polymerization is somewhat faster and semiprocessive, because although growth perturbations still occur just as in the absence of MSAs, microtubule ends transitioning to catastrophe are quickly repaired through drug binding and subsequent catching-up events. In contrast, microtubule plus ends growing in the same conditions from a stable rescue site (i.e., after a lattice defect) undergo frequent catastrophes and are not repaired through MSA binding. Therefore, in mismatching conditions, catastrophes typically evolve into long depolymerization episodes.

Importantly, microtubule severing at the site of the defect made microtubules less catastrophe-prone, in line with the view that a lattice defect at the stable rescue site has propagating properties. The underlying mechanism is unclear, but it is possible that both tubulin extension or compaction in the axial direction (51, 52) and changes in angles between protofilaments due to heterogeneity of lateral contacts (39) might play a role. One surprising feature of the drug effects in our experiments is that they can be exerted at quite low drug-binding densities (in some cases, less than one drug molecule per 8 nm of microtubule length or one tubulin “ring”). This suggests that effects of drug binding to a single tubulin dimer can propagate within the microtubule lattice. This is comparable to the reported effect of kinesin-1, where a few molecules binding to a microtubule could affect the structural properties of this microtubule (53).

The finding that lattice defects have a propagating impact on microtubule plus-end dynamics has important consequences for the concept of microtubule aging. Previous work showed that the catastrophe frequency increases when a microtubule grows for a longer time, indicating that multiple steps are needed to induce a catastrophe (5, 6, 47). However, the nature of these steps is still unclear: They may be associated with a gradual change in the microtubule end structure (e.g., more tapering) (7, 9, 42), but may also occur within the lattice. Both types of changes might play a role and, in fact, our data suggest that the mechanistic basis of catastrophe induction may differ, as precatastrophe microtubule tips can be different both in terms of drug accumulation and EB3 decay. We found that the occurrence of drug-induced lattice defects associated with protofilament number mismatch leads to catastrophe. Whether protofilament number switching occurring in the absence of MSAs can also lead to catastrophe is currently unclear and deserves further investigation. Lattice defects including switches in protofilament number have been extensively documented in previous studies (11, 14–17). Since microtubule lattice defects can accumulate over time, they could potentially contribute to microtubule aging. Repair associated with microtubule defects has been described both in vitro and in cells but, until now, microtubule lattice discontinuities have been mostly linked to the formation of GTP islands, rescues, and microtubule stabilization (19–22, 54). Here, we show that catastrophe induction is another important consequence of at least some types of lattice defects, and that lattice discontinuities can have a destabilizing effect on microtubules, a possibility that would need to be explored for defects occurring in the absence of MSAs in vitro and in cells.

It is also important to note that the drugs we employed, such as Taxol, docetaxel, and epothilone B, are either used for

therapies for cancer or considered for the treatment of neurodegenerative disorders (55–57). The concentrations of the drugs used in our assays are within therapeutically relevant ranges, and the knowledge that these drugs can differentially affect microtubule dynamics based on protofilament number preferences is relevant for optimizing their therapeutic applications.

Materials and Methods

Analysis of Protofilament Number. X-ray fiber diffraction images were collected on beamline BL11-NCD-SWEET of the ALBA Synchrotron. Purified bovine tubulin (5 mg) was diluted to a final concentration of 100 μ M in PM buffer (80 mM Pipes, 1 mM ethylene glycol-bis[2-aminoethylether]-N,N,N',N'-tetraacetic acid, 0.2 mM Tris, 1 mM dithiothreitol), containing 3 mM MgCl₂, 2 mM GTP, and the corresponding compound (200 μ M). Samples were incubated at 37 °C for 30 min to achieve maximum polymerization and then were mixed in a 1:1 volume ratio with prewarmed PM buffer containing 3 mM MgCl₂ and 2% methylcellulose (MO512; Sigma-Aldrich). Final concentrations of protein, nucleotide, and compound were 50 μ M tubulin, 1 mM GTP, and 100 μ M compound. Samples were centrifuged for 10 s at 2,000 \times g to eliminate air bubbles and transferred to a share-flow device (29, 58).

For each condition, 24 diffraction images were averaged and background-subtracted using ImageJ software (version 1.51j8; Wayne Rasband, NIH, Bethesda, MD). Angular image integrations were performed using XRTTools software (obtained upon request from beamline BM26-DUBBLE of the European Synchrotron Radiation Facility). For average protofilament number determination, image analysis was performed as previously described (59) considering the absolute position of J₀₁ for Taxol (0.0518 nm) as the reference for determining the relative peak positions for the remaining assayed conditions.

Cryo-EM was carried out as described previously (24); see *SI Appendix* for details.

In Vitro Assays of Microtubule Dynamics and Laser Ablation. In vitro assays for microtubule growth dynamics using TIRF microscopy and laser ablation were performed as described previously (24, 34, 35); see *SI Appendix* for experimental details and for details of image analysis. Photoablation assays were performed on a TIRF microscope which was equipped with an ILas System (Roper Scientific France/PICT-IBISA) and a 532-nm Q-switched pulsed laser (Teem Photonics). In vitro microtubule dynamics assays were performed in the presence of GMPCPP-stabilized microtubule seeds with 15 μ M tubulin supplemented with 3% rhodamine-tubulin and 20 nM mCherry-EB3 without (control) or with 100 nM Fchitax-3. Control microtubules were severed randomly by a 532-nm-focused laser beam. In mismatching conditions (GMPCPP seeds extended in the presence of 100 nM Fchitax-3), microtubule lattices were ablated at the site of Fchitax-3 accumulations or in the region between the seed and an Fchitax-3 accumulation.

Data Availability. The data that support the conclusions are available in the manuscript; the original fluorescence microscopy datasets are available upon request to the corresponding author. All MATLAB code, kymographs, and regions of interest used for the analysis reported in this paper have been deposited in Figshare (https://figshare.com/collections/Microtubule_lattice_defects_promote_catastrophes/5287663) (60).

ACKNOWLEDGMENTS. We thank G. F. Díaz for the calf brain supply and the staff of beamline BL11-NCD-SWEET (ALBA, Cerdanyola del Vallès, Spain) for their support with X-ray fiber diffraction experiments, Kamimura (Chuo University, Tokyo, Japan) for providing the share-flow device employed for fiber diffraction experiments, W. S. Fang (Institute of Materia Medica, Beijing, China) for providing Fchitax-3, S. Glauser and K.-H. Altmann (Institute of Pharmaceutical Sciences, ETH Zürich, Switzerland) for providing Alexa₄₈₈-epothilone B, and N. Gudimchuk (Lomonosov Moscow State University, Moscow, Russia) for helpful discussions. This work was supported by European Research Council Synergy Grant 609822 and Netherlands Organization for Scientific Research (NWO) CV ECHO Grant 711.015.005 (to A.A.), Biotechnology and Biological Sciences Research Council Grant BB/N018176/1 (to C.A.M.), and grants from Fundación TATIANA, 20202020E301 from the Spanish National Research Council, and PID2019-104545RB-I00 from Ministerio de Ciencia, Innovación y Universidades (to J.F.D.). S.W.M. was supported by a grant from the Medical Research Council, UK (to C.A.M.) (MR/R000352/1). A.R. is a recipient of a Ramalingaswami Re-Entry Fellowship, Department of Biotechnology, India.

1. A. Desai, T. J. Mitchison, Microtubule polymerization dynamics. *Annu. Rev. Cell Dev. Biol.* **13**, 83–117 (1997).
2. A. Akhmanova, M. O. Steinmetz, Control of microtubule organization and dynamics: Two ends in the limelight. *Nat. Rev. Mol. Cell Biol.* **16**, 711–726 (2015).
3. M. K. Gardner, M. Zanic, J. Howard, Microtubule catastrophe and rescue. *Curr. Opin. Cell Biol.* **25**, 14–22 (2013).
4. A. Aher, A. Akhmanova, Tipping microtubule dynamics, one protofilament at a time. *Curr. Opin. Cell Biol.* **50**, 86–93 (2018).
5. D. J. Odde, L. Cassimeris, H. M. Buettner, Kinetics of microtubule catastrophe assessed by probabilistic analysis. *Biophys. J.* **69**, 796–802 (1995).
6. M. K. Gardner, M. Zanic, C. Gell, V. Bormuth, J. Howard, The depolymerizing kinesins Kip3 (kinesin-8) and MCAK (kinesin-13) are catastrophe factors that destabilize microtubules by different mechanisms. *Cell* **147**, 1092–1103 (2011).
7. C. E. Coombes, A. Yamamoto, M. R. Kenzie, D. J. Odde, M. K. Gardner, Evolving tip structures can explain age-dependent microtubule catastrophe. *Curr. Biol.* **23**, 1342–1348 (2013).
8. H. Doodhi *et al.*, Termination of protofilament elongation by eribulin induces lattice defects that promote microtubule catastrophes. *Curr. Biol.* **26**, 1713–1721 (2016).
9. C. Duellberg, N. I. Cade, T. Surrey, Microtubule aging probed by microfluidics-assisted tubulin washout. *Mol. Biol. Cell* **27**, 3563–3573 (2016).
10. H. Sui, K. H. Downing, Structural basis of interprotofilament interaction and lateral deformation of microtubules. *Structure* **18**, 1022–1031 (2010).
11. D. Chrétien, S. D. Fuller, Microtubules switch occasionally into unfavorable configurations during elongation. *J. Mol. Biol.* **298**, 663–676 (2000).
12. S. Chaaban, G. J. Brouhard, A microtubule bestiary: Structural diversity in tubulin polymers. *Mol. Biol. Cell* **28**, 2924–2931 (2017).
13. R. A. Cross, Microtubule lattice plasticity. *Curr. Opin. Cell Biol.* **56**, 88–93 (2019).
14. D. Chrétien, F. Metoz, F. Verde, E. Karsenti, R. H. Wade, Lattice defects in microtubules: Protofilament numbers vary within individual microtubules. *J. Cell Biol.* **117**, 1031–1040 (1992).
15. I. Arnal, R. H. Wade, How does Taxol stabilize microtubules? *Curr. Biol.* **5**, 900–908 (1995).
16. J. Atherton, M. Stouffer, F. Francis, C. A. Moores, Microtubule architecture in vitro and in cells revealed by cryo-electron tomography. *Acta Crystallogr. D Struct. Biol.* **74**, 572–584 (2018).
17. B. Vitre *et al.*, EB1 regulates microtubule dynamics and tubulin sheet closure in vitro. *Nat. Cell Biol.* **10**, 415–421 (2008).
18. H. E. Foster, C. Ventura Santos, A. P. Carter, A cryo-ET study of microtubules in axons. *bioRxiv* [Preprint] (2021). <https://doi.org/10.1101/2021.03.29.437471> (Accessed 9 November 2021).
19. L. Schaedel *et al.*, Lattice defects induce microtubule self-renewal. *Nat. Phys.* **15**, 830–838 (2019).
20. L. Schaedel *et al.*, Microtubules self-repair in response to mechanical stress. *Nat. Mater.* **14**, 1156–1163 (2015).
21. C. Aumeier *et al.*, Self-repair promotes microtubule rescue. *Nat. Cell Biol.* **18**, 1054–1064 (2016).
22. A. Dimitrov *et al.*, Detection of GTP-tubulin conformation in vivo reveals a role for GTP remnants in microtubule rescues. *Science* **322**, 1353–1356 (2008).
23. G. J. Brouhard, L. M. Rice, Microtubule dynamics: An interplay of biochemistry and mechanics. *Nat. Rev. Mol. Cell Biol.* **19**, 451–463 (2018).
24. A. Rai *et al.*, Taxanes convert regions of perturbed microtubule growth into rescue sites. *Nat. Mater.* **19**, 355–365 (2020).
25. M. Zanic, J. H. Stear, A. A. Hyman, J. Howard, EB1 recognizes the nucleotide state of tubulin in the microtubule lattice. *PLoS One* **4**, e7585 (2009).
26. S. P. Maurer, F. J. Fourniol, G. Bohner, C. A. Moores, T. Surrey, EBs recognize a nucleotide-dependent structural cap at growing microtubule ends. *Cell* **149**, 371–382 (2012).
27. J. Roostalu *et al.*, The speed of GTP hydrolysis determines GTP cap size and controls microtubule stability. *eLife* **9**, e51992 (2020).
28. J. F. Díaz, J. M. Valpuesta, P. Chacón, G. Diakun, J. M. Andreu, Changes in microtubule protofilament number induced by Taxol binding to an easily accessible site. Internal microtubule dynamics. *J. Biol. Chem.* **273**, 33803–33810 (1998).
29. J. Estévez-Gallego *et al.*, Structural model for differential cap maturation at growing microtubule ends. *eLife* **9**, e50155 (2020).
30. R. Matesanz *et al.*, Modulation of microtubule interprotofilament interactions by modified taxanes. *Biophys. J.* **101**, 2970–2980 (2011).
31. A. Ginsburg *et al.*, Structure of dynamic, Taxol-stabilized, and GMPPCP-stabilized microtubule. *J. Phys. Chem. B* **121**, 8427–8436 (2017).
32. A. A. Hyman, D. Chrétien, I. Arnal, R. H. Wade, Structural changes accompanying GTP hydrolysis in microtubules: Information from a slowly hydrolyzable analogue guanylyl-(alpha,beta)-methylene-diphosphonate. *J. Cell Biol.* **128**, 117–125 (1995).
33. J. M. Andreu *et al.*, Solution structure of Taxotere-induced microtubules to 3-nm resolution. The change in protofilament number is linked to the binding of the Taxol side chain. *J. Biol. Chem.* **269**, 31785–31792 (1994).
34. P. Bieling *et al.*, Reconstitution of a microtubule plus-end tracking system in vitro. *Nature* **450**, 1100–1105 (2007).
35. R. Mohan *et al.*, End-binding proteins sensitize microtubules to the action of microtubule-targeting agents. *Proc. Natl. Acad. Sci. U.S.A.* **110**, 8900–8905 (2013).
36. Y. Komarova *et al.*, Mammalian end binding proteins control persistent microtubule growth. *J. Cell Biol.* **184**, 691–706 (2009).
37. R. A. Walker *et al.*, Dynamic instability of individual microtubules analyzed by video light microscopy: Rate constants and transition frequencies. *J. Cell Biol.* **107**, 1437–1448 (1988).
38. A. Aher *et al.*, CLASP suppresses microtubule catastrophes through a single TOG domain. *Dev. Cell* **46**, 40–58.e8 (2018).
39. G. E. Debs, M. Cha, X. Liu, A. R. Huehn, C. V. Sindelar, Dynamic and asymmetric fluctuations in the microtubule wall captured by high-resolution cryoelectron microscopy. *Proc. Natl. Acad. Sci. U.S.A.* **117**, 16976–16984 (2020).
40. D. Chrétien, S. D. Fuller, E. Karsenti, Structure of growing microtubule ends: Two-dimensional sheets close into tubes at variable rates. *J. Cell Biol.* **129**, 1311–1328 (1995).
41. J. R. McIntosh *et al.*, Microtubules grow by the addition of bent guanosine triphosphate tubulin to the tips of curved protofilaments. *J. Cell Biol.* **217**, 2691–2708 (2018).
42. P. Zakharov *et al.*, Molecular and mechanical causes of microtubule catastrophe and aging. *Biophys. J.* **109**, 2574–2591 (2015).
43. T. Kim, L. M. Rice, Long-range, through-lattice coupling improves predictions of microtubule catastrophe. *Mol. Biol. Cell* **30**, 1451–1462 (2019).
44. V. VanBuren, L. Cassimeris, D. J. Odde, Mechanochemical model of microtubule structure and self-assembly kinetics. *Biophys. J.* **89**, 2911–2926 (2005).
45. M. K. Gardner *et al.*, Rapid microtubule self-assembly kinetics. *Cell* **146**, 582–592 (2011).
46. K. J. Mickolajczyk, E. A. Geyer, T. Kim, L. M. Rice, W. O. Hancock, Direct observation of individual tubulin dimers binding to growing microtubules. *Proc. Natl. Acad. Sci. U.S.A.* **116**, 7314–7322 (2019).
47. H. Bowne-Anderson, M. Zanic, M. Kauer, J. Howard, Microtubule dynamic instability: A new model with coupled GTP hydrolysis and multistep catastrophe. *BioEssays* **35**, 452–461 (2013).
48. N. B. Gudimchuk *et al.*, Mechanisms of microtubule dynamics and force generation examined with computational modeling and electron cryotomography. *Nat. Commun.* **11**, 3765 (2020).
49. E. H. Kellogg *et al.*, Insights into the distinct mechanisms of action of taxane and non-taxane microtubule stabilizers from cryo-EM structures. *J. Mol. Biol.* **429**, 633–646 (2017).
50. E. M. Mandelkow, R. Schultheiss, R. Rapp, M. Müller, E. Mandelkow, On the surface lattice of microtubules: Helix starts, protofilament number, seam, and handedness. *J. Cell Biol.* **102**, 1067–1073 (1986).
51. R. Zhang, B. LaFrance, E. Nogales, Separating the effects of nucleotide and EB binding on microtubule structure. *Proc. Natl. Acad. Sci. U.S.A.* **115**, E6191–E6200 (2018).
52. R. Zhang, G. M. Alushin, A. Brown, E. Nogales, Mechanistic origin of microtubule dynamic instability and its modulation by EB proteins. *Cell* **162**, 849–859 (2015).
53. T. Shima *et al.*, Kinesin-binding-triggered conformation switching of microtubules contributes to polarized transport. *J. Cell Biol.* **217**, 4164–4183 (2018).
54. A. Vemu *et al.*, Severing enzymes amplify microtubule arrays through lattice GTP-tubulin incorporation. *Science* **361**, eaau1504 (2018).
55. M. O. Steinmetz, A. E. Prota, Microtubule-targeting agents: Strategies to hijack the cytoskeleton. *Trends Cell Biol.* **28**, 776–792 (2018).
56. C. Dumontet, M. A. Jordan, Microtubule-binding agents: A dynamic field of cancer therapeutics. *Nat. Rev. Drug Discov.* **9**, 790–803 (2010).
57. K. R. Brunden, V. M. Lee, A. B. Smith, III, J. Q. Trojanowski, C. Ballatore, Altered microtubule dynamics in neurodegenerative disease: Therapeutic potential of microtubule-stabilizing drugs. *Neurobiol. Dis.* **105**, 328–335 (2017).
58. S. Kamimura, Y. Fujita, Y. Wada, T. Yagi, H. Iwamoto, X-ray fiber diffraction analysis shows dynamic changes in axial tubulin repeats in native microtubules depending on paclitaxel content, temperature and GTP-hydrolysis. *Cytoskeleton (Hoboken)* **73**, 131–144 (2016).
59. R. Matesanz *et al.*, Taxanes with high potency inducing tubulin assembly overcome tumoural cell resistances. *Bioorg. Med. Chem.* **22**, 5078–5090 (2014).
60. A. Rai *et al.*, Kapitein Lab: Supplementary code, raw data and figure plots from “Lattice defects induced by microtubule-stabilizing agents exert a long-range effect on microtubule growth by promoting catastrophes.” Figshare. <https://doi.org/10.6084/m9.figshare.c.5287663.v2>. Deposited 13 November 2021.